Universita' degli Studi di Padova

SCUOLA DI SCIENZE
DIPARTIMENTO DI FISICA ED ASTRONOMIA
"GALILEO GALILEI"

LAUREA TRIENNALE IN ASTRONOMIA

The study of Newton's rings for alignment of astronomical's instruments

Relatore: Prof. Giampaolo Piotto
Correlatore: Prof. Roberto Ragazzoni

Laureanda: GIULIA SERENI

A.A. 2014 - 2015

To my parents and brother

Abstract

This thesis underlines the importance of the alignment of optical instruments as necessity for observing the Sky and scientific research. Since Newton's rings play a relevant role in the procedure of centration, my thesis focuses on the displacement of it caused by decentering of a lens. A procedure which connects this two factors is presented and verified in laboratory. In this way this thesis is a confirmation that Newton's rings are useful during alignment. Ultimately, since we know that the minor error of centration we make the best performance we get, the centering precision of the mounted lens is calculated.

In detail, Chapter 1 gives only the prerequisites useful for the understanding of the entire thesis. Chapter 2 is an excursus of actual telescopes and satellites, such as the Large Binocular Telescope and PLAnetary Transits and Oscillations of stars, whit a short description of alignment of their optical components. The formation of Newton's rings is explained in Chapter 3 both in its historical terms and as interference of two reflections.
In the laboratory, we reproduced an optical setup in order to see Newton's rings and confirm the linear relation between the decentering of a lens and the displacement of Newton's rings: this is discussed in Chapter 4. Moreover, the images and results taken with a Charge-Coupled-Device are also reported. Thanks to the data collected, in Chapter 5, we assess that the lens is aligned within a certain precision and we give future persective.

Contents

Chapter 1

Optics for astronomy

Before having the central discussion, we will review some results from geometrical optics.
Geometrical optics adopts a ray theory of light, ignoring many of its wave and all of its particle properties.

1.1 Rays in dielectric media

The speed of light in a vacuum is a constant, c. Experiments shows that the phase velocity of light waves in transparent dielectrics like air, water, or glass, is always less than c. The index of refraction measures the degree to which a particular material reduces the speed of light wave. If v is the actual speed of light in a medium (the phase velocity), then the index of refraction of the material is:

$$n(\lambda) = \frac{c}{v(\lambda)} \tag{1.1}$$

In general, n is an optical property that describes how light propagates through a material and depends on the chemical and physical (e.g. temperature) properties of the medium, as well as on wavelength. The change in index of refraction with wavelength is known as dispersion.

1.2 Laws of geometrical optics

The main laws that describe how rays propagate in a medium are the law of reflection and the Snell's law of refraction.

1.2.1 Law of reflection

Consider a reflected surface with a perpendicular axis and a ray propagating toward it at an incidence angle θ_i, conventionally measured from the normal of the interface. The ray is reflected at an angle of reflection, θ_r, given by the law of reflection:

$$\theta_i = \theta_r \tag{1.2}$$

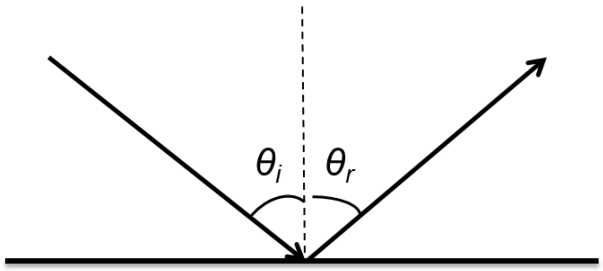

Figure 1.1: Law of reflection

1.2.2 Snell's law

With regard to refraction, Snell's law shows us that rays travelling from a lower index medium to a higher index medium will bend toward the perpendicular to the interface. Call the lower index of refraction n_1, the higher one n_2 and the angle of refraction θ_R. Snell's law states:

$$n_1 sen\theta_i = n_2 sen\theta_R \tag{1.3}$$

Figure 1.2 illustrates Snell's law.

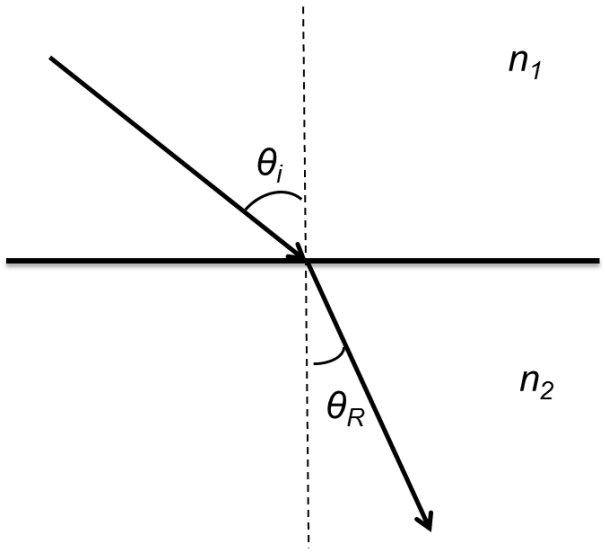

Figure 1.2: Snell's law

1.3 Spherical surface

An important result in geometrical optics describes reflection and refraction at a spherical surface.

1.3.1 Reflection from a spherical surface

We examine a concave spherical surface of radius R whose center is at C. The axis of symmetry of the system is called *optical axis* and it is marked in Figure 1.3 as horizontal dotted line. We set up a conventional Cartesian coordinate system, where z-axis is coincident with the optical axis, ad the origin is at the vertex of the mirror - point V in the figure (the intersection of the optical axis and the mirror surface). The y-axis goes upwards on the page, the x-axis outwards.

We assume *paraxial approximation*: all incident rays are nearly parallel to the optical axis and all angles of reflection are small. This latter assumption means that the diameter of the mirror is small compared to its radius of curvature. In the figure the ray, that originates at the object at point O on the optical axis, is reflected to reach the image point I. Note that $p = O\bar{V}$ is the object distance and $q = I\bar{V}$ is the image distance. After some calculation we get the *paraxial equation for mirrors*:

$$\frac{2}{R} = \frac{1}{p} + \frac{1}{q} \tag{1.4}$$

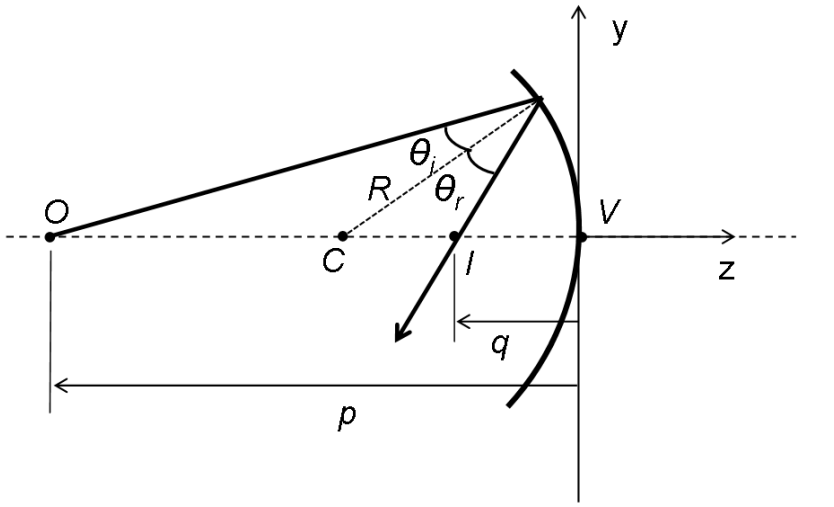

Figure 1.3: Reflection from spherical surface

The distance $R/2$ is termed the *focal length* of the mirror, and is often symbolised by f, so the above equation is usually written as:

$$\frac{1}{f} = \frac{1}{p} + \frac{1}{q} \tag{1.5}$$

Remark that if $p \to \infty$, then $q \to f$. In other words, the mirror reflects every ray arriving parallel to the optical axis to a common point.

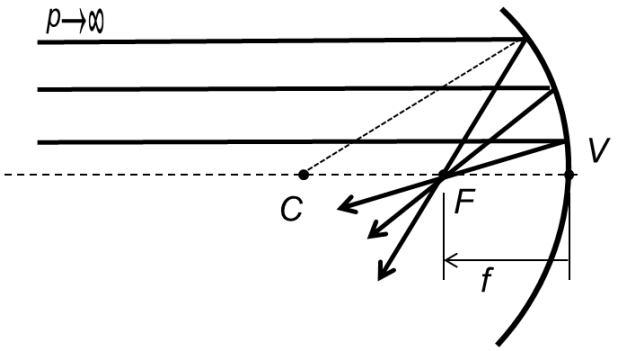

Figure 1.4: The focal point of a concave spherical mirror

More specifically, the Figure 1.4 illustrates this: a concave mirror gathers electromagnetic radiation coming from infinity and concentrate it at common focus F. Note that $\bar{FV} = f$.

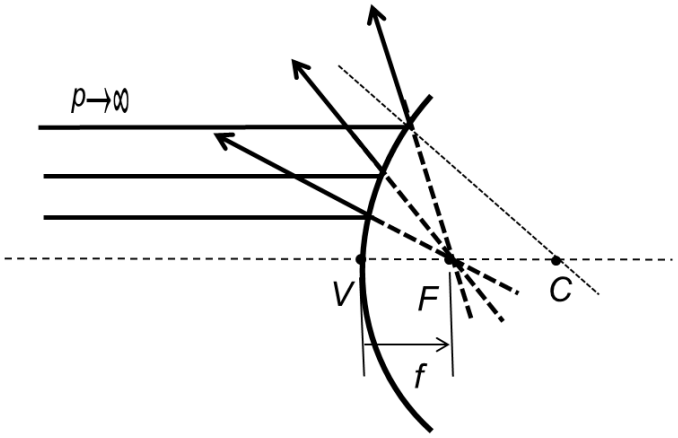

Figure 1.5: The focal point of a convex spherical mirror

On the other hand, a convex mirror, illustrated in Figure 1.5, has a positive f, meaning that the focal point lies to the right of V. Clearly, convex mirror disperses, rather than gathers, parallel rays.

1.3.2 Refraction at a spherical surface

Figure 1.6 illustrates a ray refracted at a spherical interface between media of differing indices of refraction. The paraxial equation for refraction is:

$$\frac{n_2}{q} + \frac{n_1}{p} = \frac{(n_2 - n_1)}{R_{12}} \tag{1.6}$$

Note that R_{12}, q and p are positive and $n_1 < n_2$.

As in the case of mirror, take the focal length, f_2, to be the value of q when $p \to \infty$:

$$f_2 = \frac{n_2 R_{12}}{(n_2 - n_1)} \tag{1.7}$$

Viceversa, if $q \to \infty$, then $p = f_1$

$$f_1 = \frac{n_1 R_{12}}{(n_2 - n_1)} \tag{1.8}$$

Figure 1.7 shows the focal length of a convex interface; in the same way we can illustrate the focal length of a concave surface.

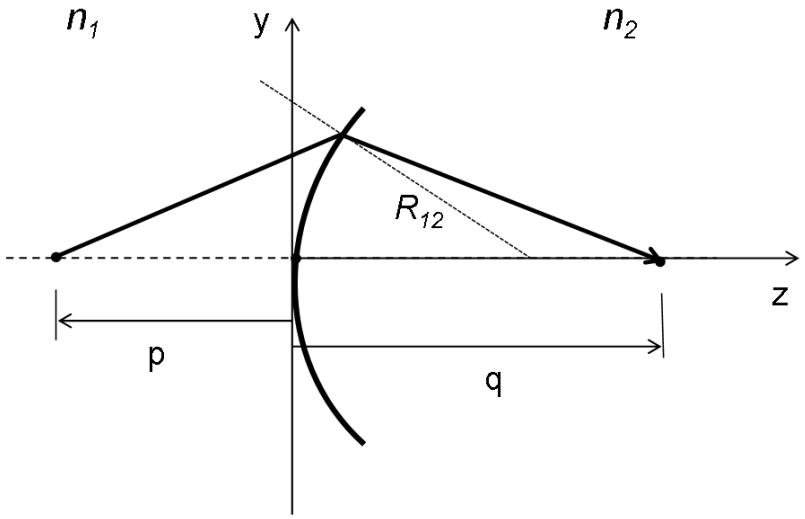

Figure 1.6: Refraction at spherical interface

1.4 Reflectance

With regard to an incident beam travelling from a medium of a given n_1 to a medium of a given n_2, the Fresnel's formula describes what fraction of the light is reflected and what fraction is refracted.
The reflectance, r, at normal incidence ($\theta_i = 0$), is given by

$$r = \left(\frac{n_2 - n_1^2}{n_2 + n_1^2}\right)^2 \tag{1.9}$$

So, when light incides to a spherical surface (assuming that its index of refraction is 1.5) the reflectance is 4%. We recall Figure 1.3. By prolonging back the reflected ray a virtual source appears; this is called ghost source.

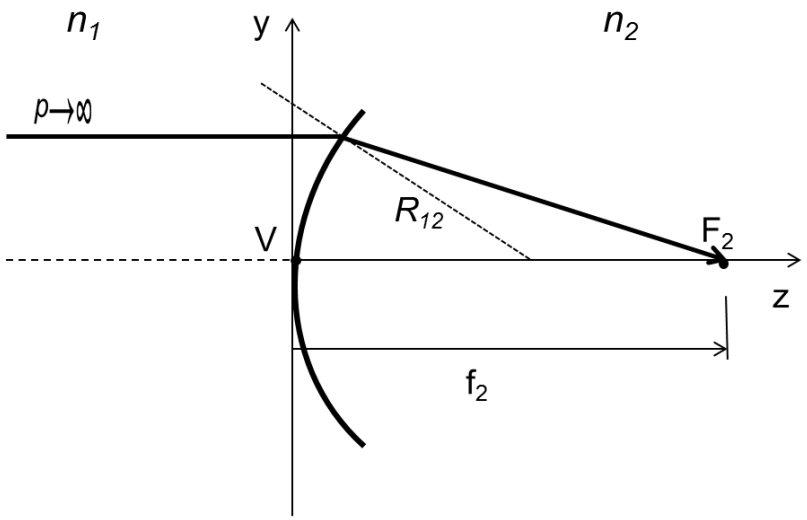

Figure 1.7: The focal length of a convex interface between media of differing index of refraction

1.5 Thin lenses

Two surfaces in succession (both spherical or one flat and the other spherical) that separate a media of n_1 and a media of n_2 constitutes a lens. A lens is called *thin lens* if the thickness (the distance along the optical axis between the two surfaces) is negligible with respect to the radii of curvature, the focal length and the object, image distances. In other word, we ignore what happens inside the lens.
Two types of lens exist and are illustrated in the Figure 1.8:

- *convergent lens* such as double convex lens, plano convex lens, convergent meniscus
- *divergent lens* such as double concave lens, plano concave lens, divergent meniscus.

The paraxial equation for a thin lens can be derived easily by imposing two paraxial equations for each surface. Call the radii of the first surface, R_{12} and

the radii of the second surface, R_{23}. We get:

$$\frac{1}{q} + \frac{1}{p} = (n_2 - n_1)\left(\frac{1}{R_{12}} - \frac{1}{R_{23}}\right) \tag{1.10}$$

As we did before, if $p \to \infty$, then all rays converge to the same common point and $q = f'$. Therefore the focal length:

$$\frac{1}{f'} = (n_2 - n_1)\left(\frac{1}{R_{12}} - \frac{1}{R_{23}}\right) \tag{1.11}$$

It is intuitive that the focal length of a thin lens is only one. For a convergent lens $f' > 0, R_{12} > 0, R_{23} < 0$; on the contrary, for a divergent lens $f' < 0, R_{12} < 0, R_{23} > 0$. In a convergent meniscus $R_{23} > R_{12} > 0, f' > 0$ and in a divergent meniscus $0 < R_{23} < R_{12}, f' < 0$. Definitely, the paraxial or Gaussian formula for thin lens is:

$$\frac{1}{q} + \frac{1}{p} = \frac{1}{f'} \tag{1.12}$$

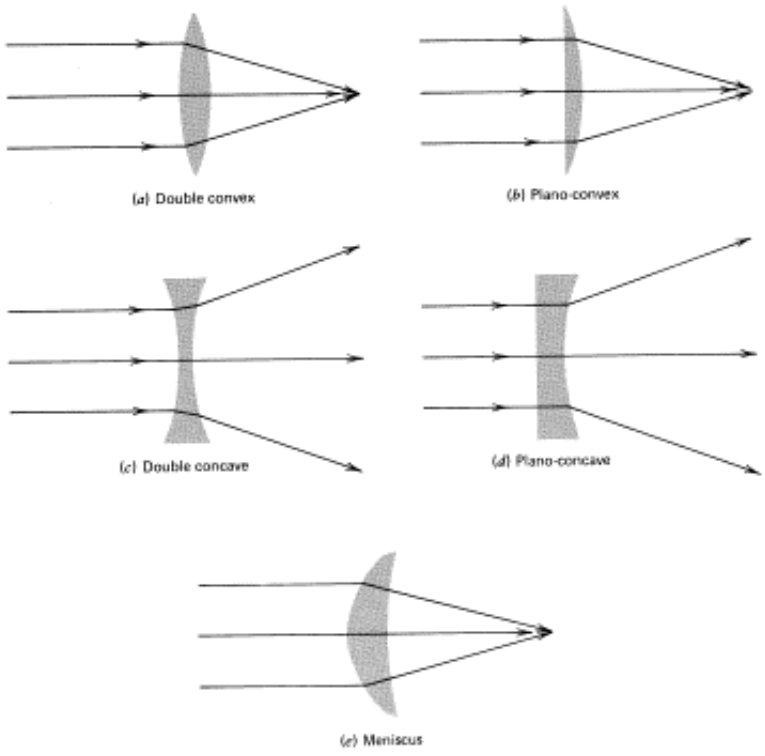

Figure 1.8: Different type of lenses: convergent and divergent.

1.6 Image quality: the Airy disk

The wave properties of light set a fundamental limit on the quality of an optical system's image. Wavefronts from a point source arrive at a parabolic mirror as parallel surfaces. The parabolic shape of the mirror converts the incoming flat wavefronts into reflected spherical wavefronts. These spherical wavefronts converge at the focal point of the mirror. If the mirror was perfect, diffraction did not exist, the focal point would be infinitesimally small. We recall Figure 1.4.

Indeed we know that no perfect mirror without imperfections exist. When light meets the edge of an optical component, specifically a concave mirror, some of the energy tries to bend round it as in Figure 1.9. The diffraction of a plane wavefronts happens at the edges of the mirror. So, the diffracted wavefronts will interfere as in Figure 1.10.

Despite the fact that the source is a point, its image will have a finite size: the majority (84%) of the light focuses into a spot or "disk". Concentric bright rings, whose brightness decreases with distance from the center, surround the very bright central spot, the *Airy disk*. The angular diameter of the dark ring

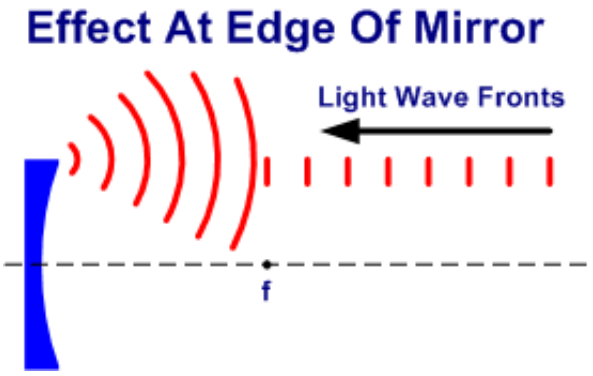

Figure 1.9: Diffraction by the edge of a mirror.

that borders the Airy disk (in the figure 1.10 the blue dotted lines) is:

$$\alpha_A = \frac{2.44\lambda}{D}[radians] \tag{1.13}$$

where D is the diameter of the mirror and λ is the wavelength of the incoming light.

In conlusion, we would like to underline that this phenomena occur even with a lens. We have already marked that a lens is composed of two surfaces. The first surface causes the interference and the Airy disk forms.

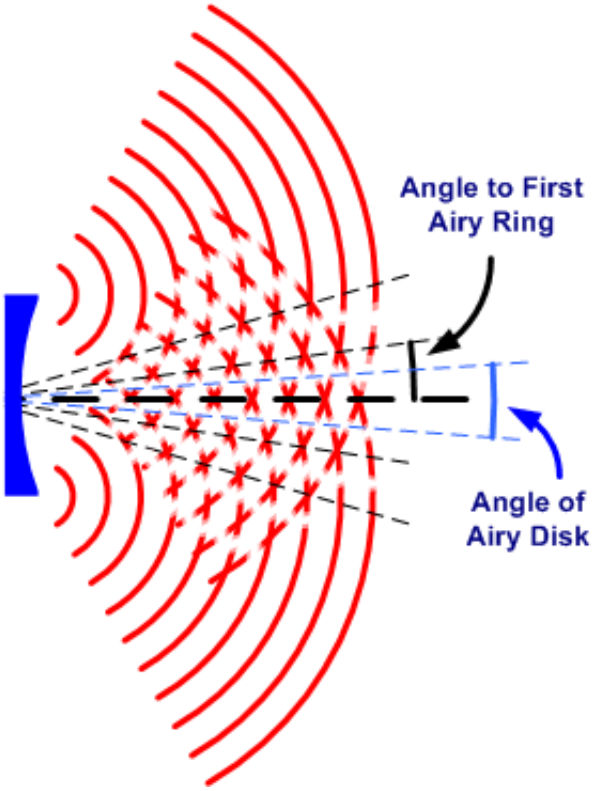

Figure 1.10: Interference of two diffracted wavefronts.

Chapter 2

The importance of alignment

Finding out new astronomical objects, answering to the questions about the Universe is one of the most fascinating thing for human being. Telescopes play a crucial role in order to pursue this goal: lenses have to be good fabricated and perfectly aligned in an optical system. AIV, Assembly Integration and Verification includes the procedure of alignment. During this procedure Newton's rings appear, so they can be used to achieve the best performance for a telescope.
We wil give some example of optical systems, such as:

- the Large Binocular Camera, LBC, installed at the prime focus station of the Large Binocular Telescope;
- the Telescope Optical Unit, TOU, installed in the PLAnetary Transits and Oscillations of stars.

2.1 LBT

LBT is the result of an Italian, German and American collaboration. The telescope is located on mount Graham, in Arizona at 3192 m of altitude. The LBT Scientific Advisory Committee (SAC) has developed the following list of observational priorities to guide the telescope design:

- Interferometric Imaging 0.4 to 400 μm
- Infrared Imaging / Photometry 2.0 to 30 μm
- Wide Field Multi-object Spectroscopy 0.3 to 1.6 μm
- Faint Object / Long Slit Spectroscopy 0.3 to 30 μm

- High Resolution Spectroscopy 0.3 to 30 μm

It can observe the Universe from the earliest epochs of galaxy formation and so, it can learn about processes of star formation and faint galaxy evolution. It can also provide a study of exo-solar planets with the possibility of life outside our solar system.

2.1.1 Structure and movement

The short focal length of the primary mirrors (F/1.142 [1]) permits a compact, quite stiff telescope structure. The base is a concrete pier 20 meters high and 14 meters in diameter, resting on the mountain bedrock. The telescope mass is approximately 580 metric tons. The telescope in Figure 2.1 is an altitude-azimuth [2] design: it uses an elevation over an azimuth mounting. It addresses any point on the sky by tipping to the correct angle

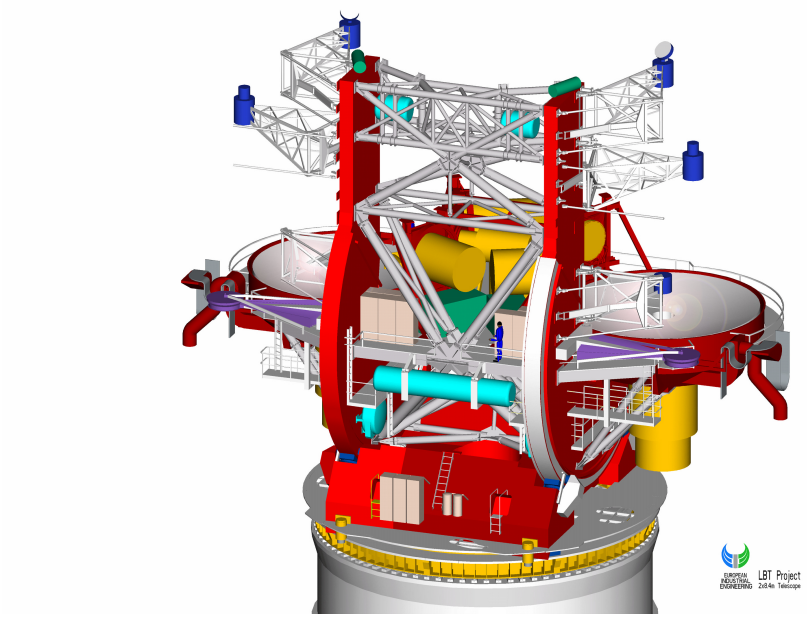

Figure 2.1: Structure of LBT

between zenith and horizon, and rotating around its vertical axis to the correct heading. So, this type of mounting requires a movement in both axes

[1] focal ratio is the ratio of the focal length of the telescope related to its aperture. It's calculated by dividing the focal length by the aperture. So in our case the focal lenght of the primary mirror is 9.6 m.

[2] Azimuth is the angular distance measured clockwise from nord; altitude is the angular distance measured from the horizon toward zenith.

to follow the scientific object, but it is not able to chase any target at zenith. The elevation optical support structure moves on two large C-shaped rings and the compact azimuth platform transmits the loads directly down to the pier.

2.1.2 Optical components

The Large Binocular Telescope uses two 8.4 m, F/1.142 primary mirrors to provide a collecting area equivalent to an 11.8 meter circular aperture. By having both the primary mirrors on the same mounting (binocular arrangement), the telescope is able to have a resolving power corresponding to a 22.8-meter telescope, or 10 times sharper than the Hubble Space Telescope.

2.1.3 The primary mirrors

The features of the primary mirros are described in the table below:

Features of primary mirrors	
Number of primary mirrors	2
Primary spacing	14.417 m center-to-center
Primary physical diameter	8.417 m
Primary focal ratio	F/1.142
Central hole physical diameter	0.889 m
Primary figure	Parabolic
Primary construction	Cast borosilicate honeycomb
	28 mm faceplate thickness
	Edge thickness 894 mm, plano-concave
Primary Mirror Mass	$\simeq$ 16 metric tons each

The main feature of borosilicate honeycomb primary mirror are:

- relatively low coefficient of thermal expansion.
- the coefficient of thermal expansion (CTE) is $2.8 \cdot 10^{-6}$/C.
- the working point is low enough that we can mold it into the complex honeycomb structures at temperatures which are easy to obtain.
- a good resistance to attack by chemicals. This property is important because the polished glass surface is recoated with a fresh coating of aluminum every one to three years. Strong acids and/or bases are used to dissolve the previous coating and contaminants. The mirrors

must survive this cleaning process dozens of times without requiring the precise surface to be re-polished.

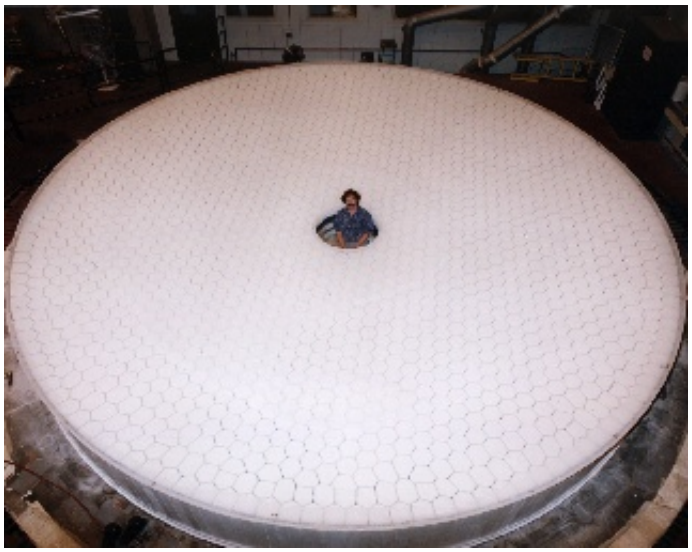

Figure 2.2: Honeycomb primary mirror

These primary mirrors were mounted and aligned in the telescope atop Arizona's Mt. Graham in 2004. In 2005, a thin coating of aluminum was applied making them highly reflective and ready for capturing images.

2.1.4 Adaptive secondary mirror

In 2010 Adaptive Optics, AO was incorporated into the design of the LBT. The telescope AO system compensates for the blur of the Earths atmosphere that causes the distortion of the wavefront coming from the source. It uses two innovative key components, namely an adaptive secondary mirror and a high-order pyramid wavefront sensor. The mirror surface changes shape typically 1000 times a second. Notice that having the telescopes secondary mirror serve as the AO deformable mirror avoids the introduction of substantial thermal background noise. It is controlled by 672 electromagnetic actuators, with magnets glued directly onto its back surface. With AO, LBT surpassed Hubble sharpness (at certain light wavelengths), achieving a Strehl ratio of $60 - 80\%$ rather than the $20 - 30\%$ of older adaptive optic systems, or the 1% typically achieved without adaptive optics for telescopes of this size.

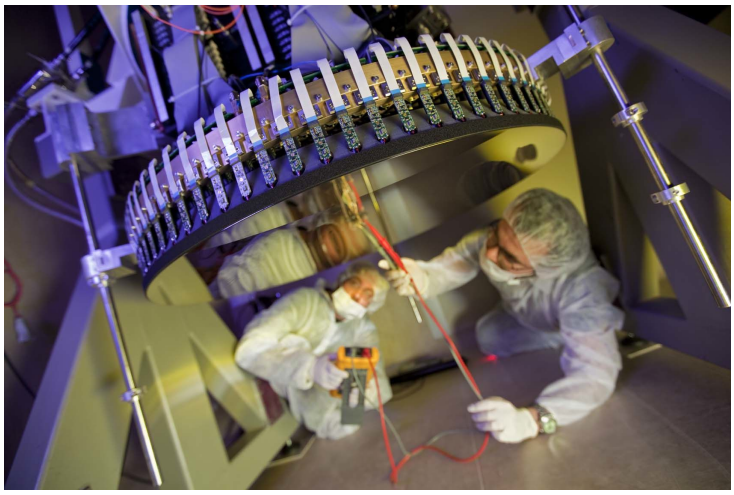

Figure 2.3: Adaptive secondary mirror

2.1.5 Optical Path Configurations

Each telescope is a Gregorian one: it has characterized by a primary parabolic concave mirror and a secondary ellipsoid concave mirror. LBT has different focal stations: Prime focus, Direct Gregorian focus, Bent Gregorian focus through the terziary mirror (or Nasmyth focus).

- *Prime focus*: the light rays hit the primary mirror, they converge to a focus, F, before they are reflected by the secondary mirror. See Figure 2.4.

- *Gregorian focus*: the reflected beam focuses to a second point G, through a hole in the centre of the primary. Hence the image forms behind the primary mirror as in a Cassegrain telescope, but it is an upright image. See Figure 2.5.

- *Bent Gregorian focus*: the reflected beam from the secondary mirror is deviated by a flat tertiary mirror inclinated of 45 with respect to the optical system axis. Hence the light diverts to Bent Gregorian foci, the so called Nasmyth focus in the very center of the telescope structure. See Figure 2.6.

Instruments mounted on swing arms above the mirrors can be used to quickly change the configuration of the telescope, to switch the telescope from one mode of observation to another very quickly.

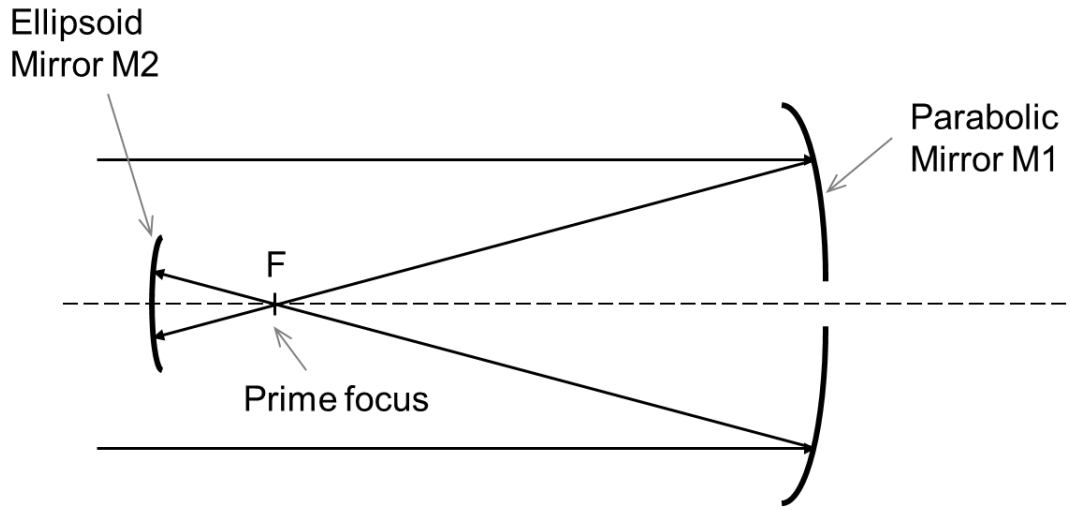

Figure 2.4: Prime focus of LBT

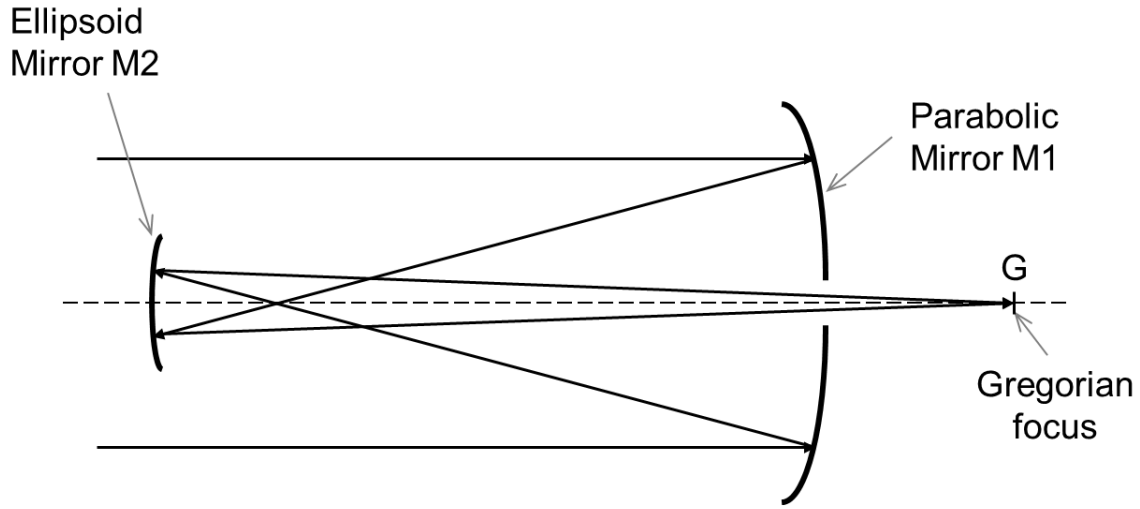

Figure 2.5: Gregorian focus of LBT.

2.1.6 Supplementary instruments

The following facility instruments are implemented on the baseline telescope:

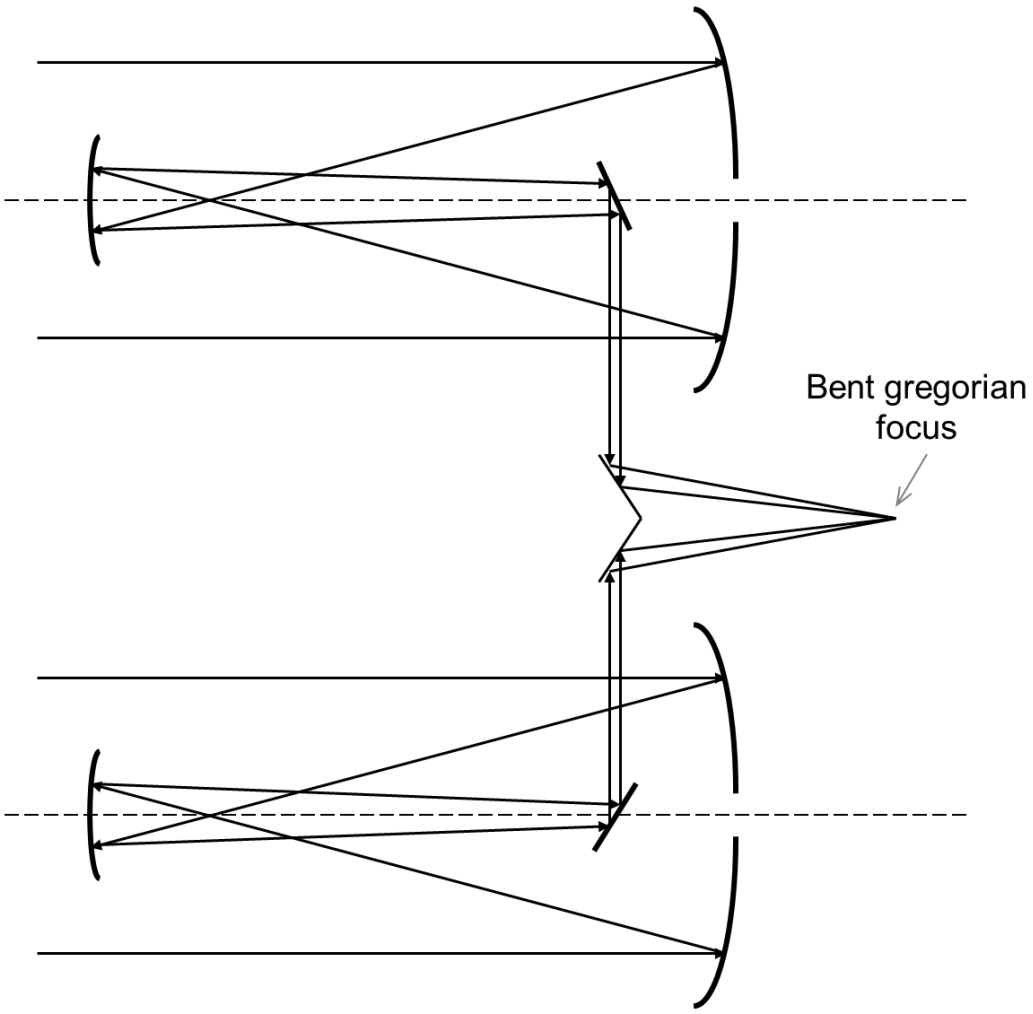

Figure 2.6: Bent gregorian focus of LBT.

- *LBC:* Large Binocular Cameras.
- *LUCIFER:* Lbt Utility Camera (and Spectrograph) Imaging Fields for Extragalactic Research.
- *MODS:* Multi-Object Double Spectrograph.
- *PEPSI:* Potsdam Echelle Polarimetric and Spectroscopic Instrument.
- *LBTI:* Large Binocular Telescope Interferometer.
- *LINC-NIRVANA:* Lbt Interferometric Camera/Near-IR and Visible Adaptive interferometer for Astronomy.

These instruments makes the LBT versatile and permits to pursue the principal goals defined by SAC.

2.1.7 LBC

The Large Binocular Camera is a double Charged-Couple-Device, CCD imager, installed at the prime focus stations of the two $8.4\,m$ telescopes of LBT, able to obtain deep and wide field images in the whole optical spectrum from UV to NIR wavelengths. The two channels, called Blue and Red, are optimized for the UB and VRIZ bands respectively and are characterized by two optical correctors with very fast focal ratio (F/1.45), specifically a modified Wynne corrector.
The Wynne scheme consists in a system of two afocal spherical lenses which are able to correct the spherical aberration and coma, and of a positive spherical lens, which is able to correct astigmatism caused by the previous lenses.
For LBC, this optical corrector balances the aberrations induced by the focal ratio (F/1.14) parabolic primary mirror of LBT. Each corrector uses six lenses with the first having a diameter of 80 *cm*. Two filter wheels allow the use of 8 filters; both narrow and broad band filters are available. Figure 2.7 illustrates the optical design: two meniscus, a plano concave, a plano-convex, a biconvex lens, the filter and a meniscus in sequence. The optical prescription data

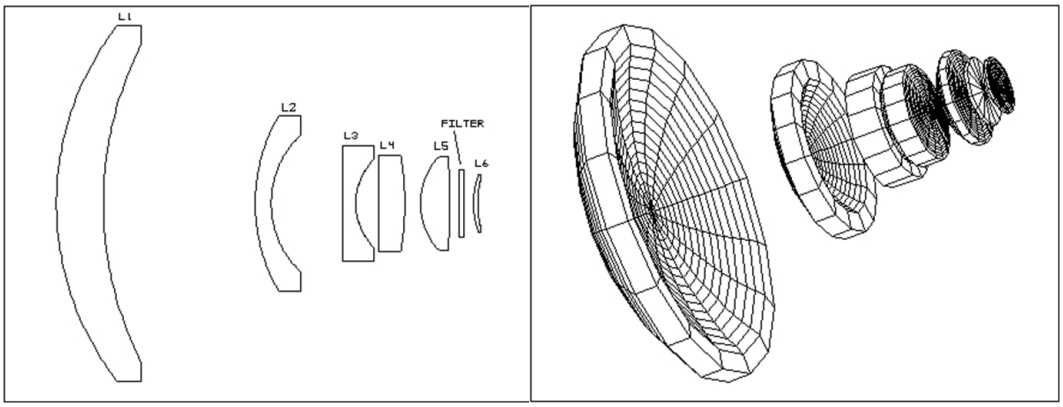

Figure 2.7: The corrector for LBC.

of the Blue channel prime focus corrector are listed in Table 2.8: The lens' surfaces are all plano or spherical with the exception of L3 characterised by an aspherical surface on its concave part. In effect L3 has an ellipsoidal surface which presents an edge deviation from a spherical surface of about 0.7 *mm*: Figure 2.9 shows this deviation. The two channels have similar optical

Comment	Radius	Thickness	Glass	Diameter	Conic
OBJECT	Infinity	Infinity		0	0
PRIMARY MIRROR	19200	8724.3	MIRROR	8404.013	-1
L1	658.9	107.0703	SILICA	810	0
	797.972	345.995		720	0
L2	397.93	36.18359	SILICA	400	0
	214.306	162.2794		310	0
L3 (ASPHERIC)	Infinity	30	SILICA	260	0
	131.77	52.08474		200	-0.586
L4	Infinity	60	SILICA	220	0
	-658.9	36		220	0
L5	156.35	66.93385	SILICA	216	0
	-1185.9	22		216	0
FILTER	Infinity	8.5	SILICA	155	0
	Infinity	22.89941		155	0
L6	184.003	10	SILICA	130	0
	233.68	15		120	0
IMAGE	Infinity			108.357	0

Figure 2.8: The optical features of Blue LBC; the units are mm.

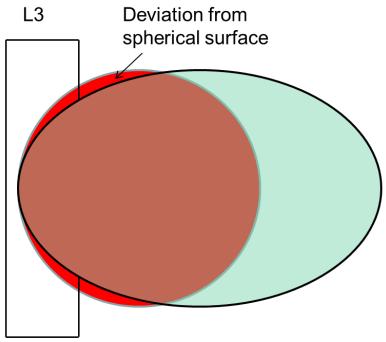

Figure 2.9: Aspherical surface of L3.

designs satisfying the same requirements, but differ in the lens glasses: fused silica for the "blue" arm and BK7 for the "red" one.

Main parameters of the optical corrector for Blue LBC	
Focal length	12180 mm
Focal ratio	$F/1.45$
Pixel size	$0.23''$
Unvignetting FoV [3]	$27'$

The increasing of the focal ratio with respect to the focal ratio of the primary mirror is greater than what we expected from Wynne scheme. This increasing of the focal length (the optical corrector) allows a better Point Spread Function sampling (PSF), assuring that the 80% of the PSF encircled energy falls inside a single CCD pixel (13.5 μm in size) for more of the 90% of the field.

In conclusion, it is necessary to align all these six lenses in order to get the best performance for LBC and LBT.

The alignment of LBC

A detailed analysis has been performed to assess the alignment tolerances that must be fulfilled in order to have a performance degradation (in terms of root mean square, RMS spot size) within 10% from the nominal value. The tightest tolerances are:

- $\pm$ 0.035 mm on the decenter of lens no. 2
- $\pm$ 18$''$ on the tilt of lens no. 1.

The first step in the system alignment is the selection of the optical axis: a suitable choice is represented by the mechanical axis of the derotator bearing, which may be materialized by a laser beam. Then the optical axis of each lens has to be aligned with the instrument optical axis, keeping the tilt and decenter errors within the specified tolerances. Each lens is mounted into a cell starting from the smallest (lens no. 6) to the largest (lens no. 1): in this step it ca be aligned with respect to tilt, measuring the misalignment errors by mechanical methods. Then the cell is fixed to the hub [4]. The remaining decenter error may be measured and then corrected referring to the laser beam which defines instrumental optical axis. In particular ghost reflections of the laser beam on the lens surfaces can be used. Moreover the shape of the resuting Newton's rings can be used to detect decentering and tilt errors. Notice that when one element is aligned, a new lens is mounted. The laser beam materializing the optical axis crosses all the lenses mounted up to a given point; in this way the misalignment errors are not indipendeten and we may state that the alignment of each lens tendo to correct the alignment errors of the revious lenses.

2.2 PLATO

PLATO is a space mission. In februar 2014, it has been selected as M3 - the third medium-class mission in ESA's Cosmic Vision Programme. Its scientific objectives are:

- find and study a large number of extrasolar planetary system

[4]The hub is the structural component of the instrument. It allows to connect the lens mounting frames into a single unit,on which the field rotator is mounted.

- detect terrestrial exoplanets in the habitable zone around solar-like stars and characterise their bulk properties
- provide the key informations needed to determine the habitability of these new worlds: planet radii, mean densities, stellar irradiation, age of planet host star and architecture of planetary systems.

PLATO is planned to be lunch in 2022 and the operation will start in Sun-Earth Lagrangian point, L2. The mission life time is expected to be longer than 6 years.
PLATO is based on a multi-instruments approach: it is composed by 32 cameras, which are defined as "Normal Cameras", observing in a very broad band ($500 - 1000\ nm$) and 2 specialized cameras, which are defined as "Fast Cameras", observing with high cadency in two broad bandpasses (blue and red). The disposition of the cameras on the optical bench has been optimized for the overlapping line of sight strategy. See Figure 2.10. The 32 cameras

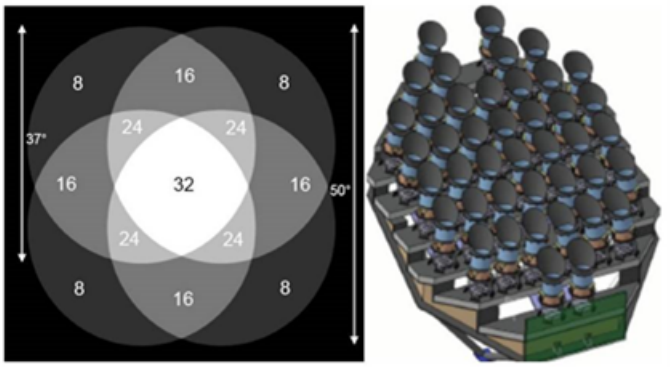

Figure 2.10: the overlapping line of sight scheme of PLATO

have been divided in four subsets of eight cameras. The Focal Plane Array, FPA is composed by four detectors. Each subset looks at the same circular Field of View, FoV. The line of sight of the four subsets are misaligned in such a way that the overlapping FoV areas guarantee the required number of stars at given noise level and the required number of stars at given magnitude (the overall FoV is 2180 degree). Look at Figure 2.11. Moreover, the overlapping line of sight strategy allows continuous observation of the same sky area with 90 degrees field rotation every 3 months. A s result, it will be cover the 50% of the sky. Each Camera is made by a Telescope Optical Unit, TOU, assembled with a Focal Plane Unit, FPU. The optical concept of the TOUs is based on a design with 6 fully centred, spherical lenses, except the first one which features an aspheric face. A front window protects the lenses form radiations

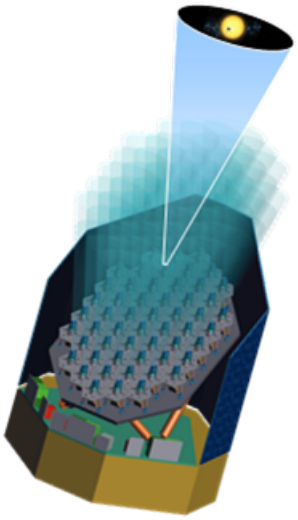

Figure 2.11: The multi telescope PLATO

and limits the sensitivity of the telescope to the thermal environment. The inner pupil, which limits the measured photometric flux, is well delimited by a circular diaphragm. Each telescope is equipped with a baffle around the front window lens. A summary of the requirements for the optical design are reported in Table.

Requirements and Drivers for the Optical Design of TOU	
Spectral range	$500 - 1000\ nm$
Entrance pupil diameter	$120\ mm$
FoV	$> 1000\ degrees$
Detector format	$4510 \times 4510\ pixels$
Pixel size	$18\ \mu m$
FPA size	$164\ mm$
Weight (lenses)	$< 6\ Kg$

Figure 2.12 shows the opto-mechanical design of TOU and Figure 2.13 illustrates the specifications of its lenses: An amount of 10% vignetting [5] at edge of the Field of View has been considered to be acceptable: tacking into account that 3% vignetting is due to the solid angle under which the pupil is seen at the edge of the field, the aperture of the first lens has been reduced in order to have a 7% vignetting at the edge of the field.

[5] Vignetting is the term used to describe a situation in an optical system where the field of view is not fully illuminated at the edges.

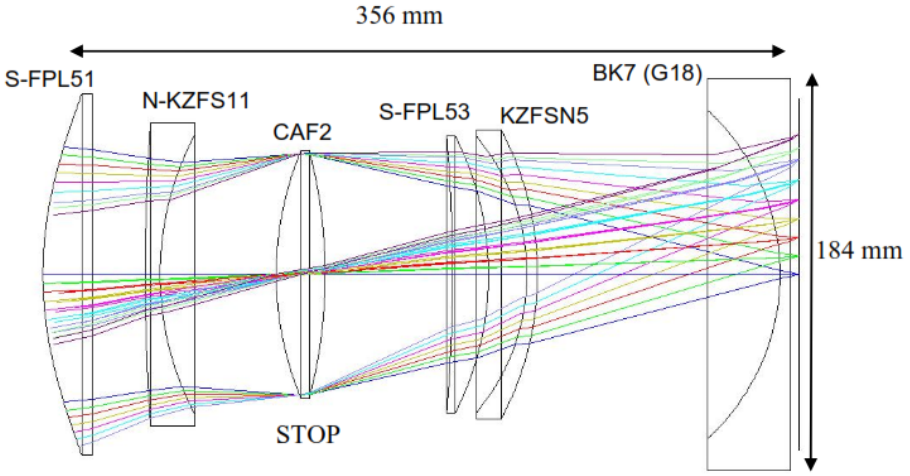

Figure 2.12: The optical design of TOU

		R (mm)	Thickness (mm)	Glass	K	a^4	a^6	shape	size (mm)
Lens 1	S1	175.662	23.000	S-FPL51	-3.766	3.952E-8	-4.480E-12	circular	169.2
	S2	infinity	25.122						
Lens 2	S3	1009.882	7.000	N-KZFS11				circular	142.0
	S4	140.090	54.635						
Lens 3	S5	150.372	23.000	CAF2				circular	116.0
	S6	-228.098	59.880						
Lens 4	S7	-791.190	17.000	S-FPL53				circular	130.0
	S8	-142.755	18.044						
Lens 5	S9	-100.445	5.000	KZFSN5				circular	136.0
	S10	-143.002	114.184						
Lens 6	S11	-103.992	5.000	BK7 (G18)				circular	184.0
	S12	infinity	4.000						
FPA	S13	infinity						square	164.4×164.4

Figure 2.13: The main Parameters of the TOU optical design.

The alignment of TOU

A prototype of one telescope unit has been built initially to show the alignment feasibility and to get the decenter and tilt misalignment sensitivity. The lenses mounted on this prototype, should have, as much as possible, the same curvature of the final design lenses. The Figure 2.14 illustrates the TOU prototype alignment setup. The detectors are conveniently mounted on linear stages which can move along the optical axis, in order to position them in correspondence of the position where the transmitted and back-reflected

spots shall focus. A variable diameter iris is inserted on the collimated beam, to maximize the transmitted and back-reflected spot sharpness and visibility.

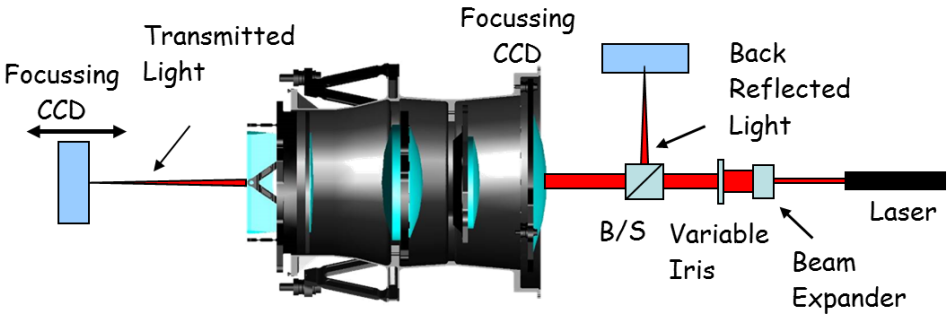

Figure 2.14: the TOU prototype alignment setup.

By using Airy and Newtons rings both of the back reflected and of the transmitted light (introducing one lens at a time) the alignment procedure of the TOU prototype will be performed. From the test setup it can be learnt that the *final alignment tolerances* are:

- centering sensitivity is always below 50 μm
- tip-tilt sensitivity is always below 50″

So if TOU is mounted with this decentering and tip-tilt sensitivity, it will pursue the best performance. Furthermore, the second step is to perform the real final alignment procedure and test in cold and warm conditions the optical performance of the system.

Chapter 3

Newton's rings

In 1717, Isaac Newton first analyzed an interference pattern caused by the reflection of light between a spherical surface and an adjacent flat surface. Although first observed by Robert Hooke in 1664, this pattern is called Newton's rings, as Newton was the first to analyze and explain the phenomena. Newton's rings appear as a series of concentric circles centered at the point of contact between the spherical and flat surfaces. When viewed with monochromatic light, Newton's rings appear as alternating bright and dark rings.

3.1 The standard setup to observe Newton's rings

Consider a spherical lens placed on the top of a flat [1] glass surface. A thin air film is formed between the plate and the lens. The lens plate system is illuminated with monochromatic light falling on it normally.

Figure 3.2 shows how the incident ray, ray 1 propagates into the described system: it gets partially reflected (ray 2) at the bottom curved surface of the lens, and part of the transmitted ray is partially reflected (ray 3) from the top surface of the plane glass plate. Since the splitted rays are coherent [2] interference occurs. We remember that the path length difference between the two reflected rays is $\Lambda = 2n_2 t \cos\theta_i$; since ray 1 incides normally, $\theta_i = 0$, then $\Lambda = 2n_2 t$. Furthermore, the phase difference is related to the path length

[1] A surface is considered to be flat when its distortion is less than lamda/4 with respect to a perfect flat surface

[2] This means that the waves from the sources must maintain a constant phase relation. For example, if two waves are phase shifted by $\varphi = \pi$,this phase shift must not change with time.

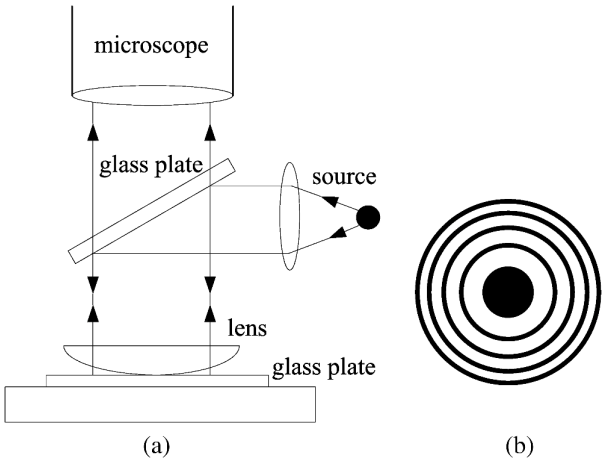

Figure 3.1: The experimental setup to observe Newtons rings.

difference by the relation $\delta \sim \Lambda \pm \pi$. At the point of contact of the lens with the glass plate the thickness of the air film is very small compared to the wavelength of light therefore the path difference introduced between the interfering waves is zero. Consequently, the interfering waves at the centre are opposite in phase (π radians out of phase) and interfere destructively. The condition of destructive interference is given by:

$$2n_2t = m\lambda \tag{3.1}$$

where m is called the order number, $m = 0, \pm1, \pm2, ..$ and n_2 is the index of refraction of the lens. Thus a dark spot is produced.

On the contrary, the condition for constructive interference is given by:

$$2n_2t = (m + \frac{1}{2})\lambda \tag{3.2}$$

In this case, the reflected waves are in phase with one another and they create a bright fringe.

In other word, the thin film has a varying thickness, so we have different interference conditions at different thicknesses. This leads to the alternating fringes of constructive interference (bright rings) and destructive interference (dark). For this reason rings are called fringes of equal thickness. We can use these rings to determine the radius of curvature of the lens surface. With reference to the Figure NRformation.jpg the relation between the distance r and t is $r^2 = R^2 - (R - t)^2 = 2Rt - t^2$. Since $R >> t$ we get:

$$r^2 = 2Rt \tag{3.3}$$

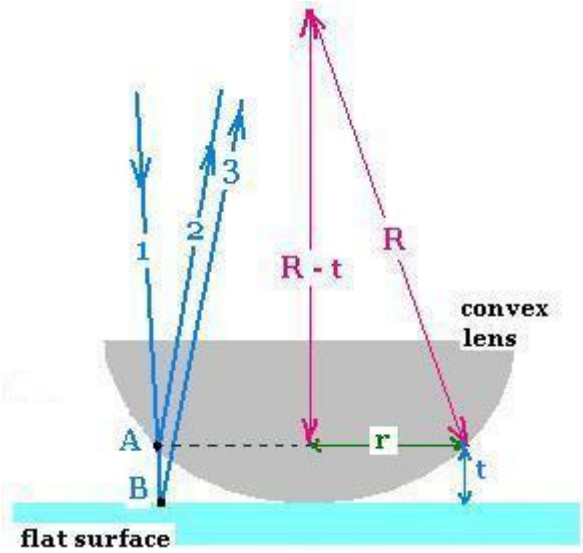

Figure 3.2: The formation of Newton's rings by a spherical lens in contact to a plate glass.

Then, by using the condition of interference, the radius of the m^{th} dark ring is given by:

$$r_m = \sqrt{mR\lambda} \tag{3.4}$$

and the radius of the m^{th} bright ring is:

$$r_m = \sqrt{(m + \frac{1}{2})R\lambda} \tag{3.5}$$

Notice that the outer rings are spaced more closely than the inner ones because the slope of the curved lens surface increases outwards.

3.2 A modern view of Newton's rings

Until now, we have seen that light, reflecting from only one surface of a lens, generates an Airy disk; we recall Figure 1.10.

Indeed, if we consider a thin lens with its two surfaces and its optical axis coinciding with a laser beam, the lens undergoes a reflection from each surface. Figure 3.3 illustrates this phenomena by neglecting what happens inside the lens. Therefore the two reflections interfere and Newton's rings appear. A lens is considered aligned when Newton's rings are perfectly concentric.

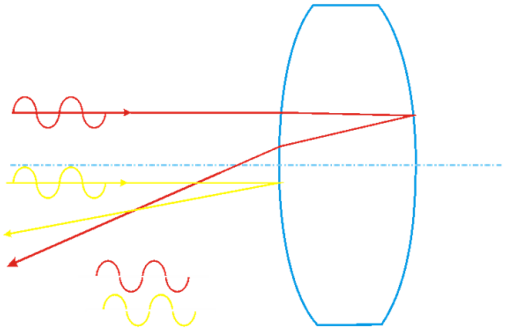

Figure 3.3: Interference of two reflections due to two surfaces of a thin lens.

3.2.1 An explicit example of a biconvex lens

Let us consider a simple system, with laser and a biconvex lens; the lens has a center thickness $d = 2.2\ mm$, but it can be seen as a thin lens with radii of curvature $R_{12} = 258\ mm$ and $R_{23} = -271\ mm$. During the procedure of mounting and alignment, a laser is mounted with respect to a system of coordinates (x, y, z): the laser beam materializes a reference axis, parallel to the optical table. So two coordinates (x, y) are fixed as illustrated in Figure 3.4. Then, the lens is placed mechanically, as much as possible, with its centre

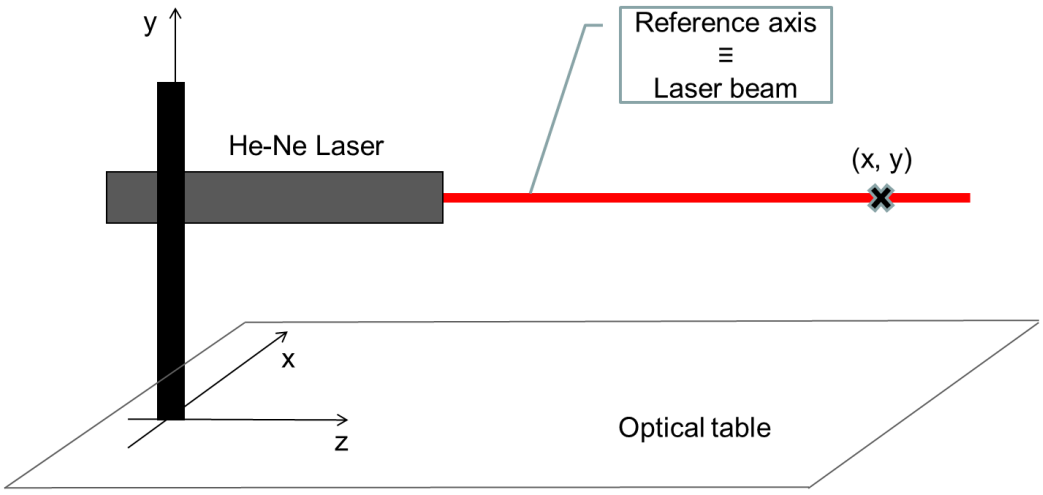

Figure 3.4: The reference axis for alignment.

in (x, y). This is the first cause of errors: by analysing the light coming in and out, optical axis could not coincide perfectly with the reference axis. Figure 3.5 and 3.6 shows what happens when a lens is decenter and tilt with respect to the reference axis (laser beam). By using Newton's rings and the

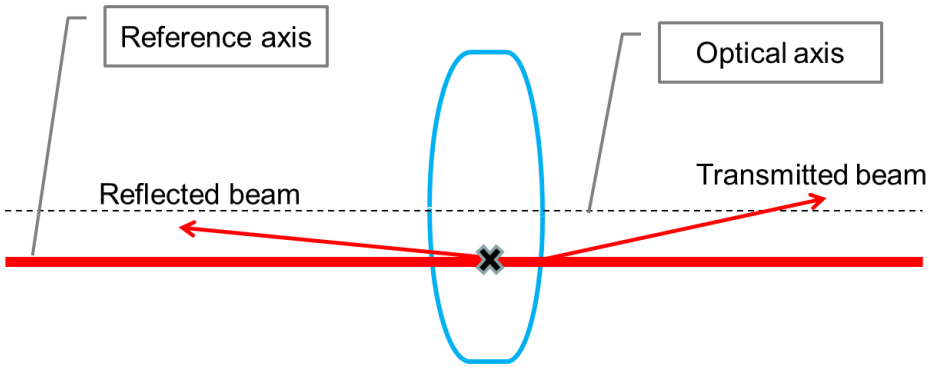

Figure 3.5: A qualitatively decentering of a lens.

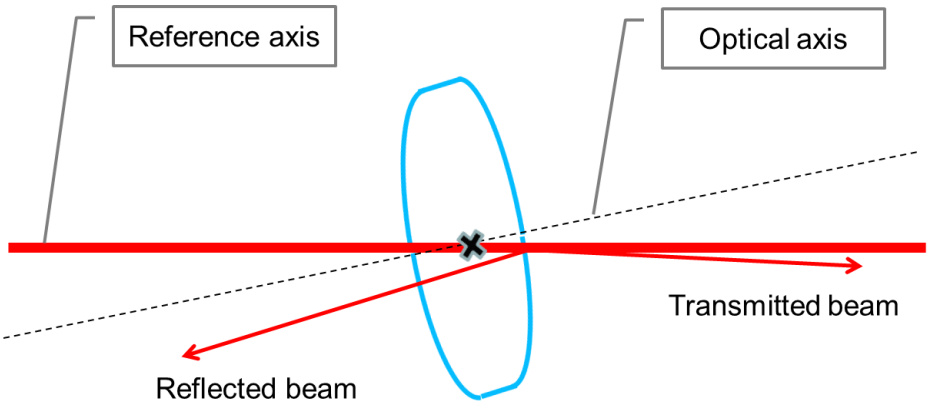

Figure 3.6: A qualitatively tilt of a lens.

adjustments, the lens will be neither inclined nor decentered with respect to a position of centration.

In order to study how Newton's rings originate, we consider two reflections due to the first and second surface of our thin lens. We recall subsection 1.3.1. Initially the laser rays hit the first surface, S_1 and it reflects off S_1 as in the Figure 3.7 If we trace the reflected rays backward to a common point, the

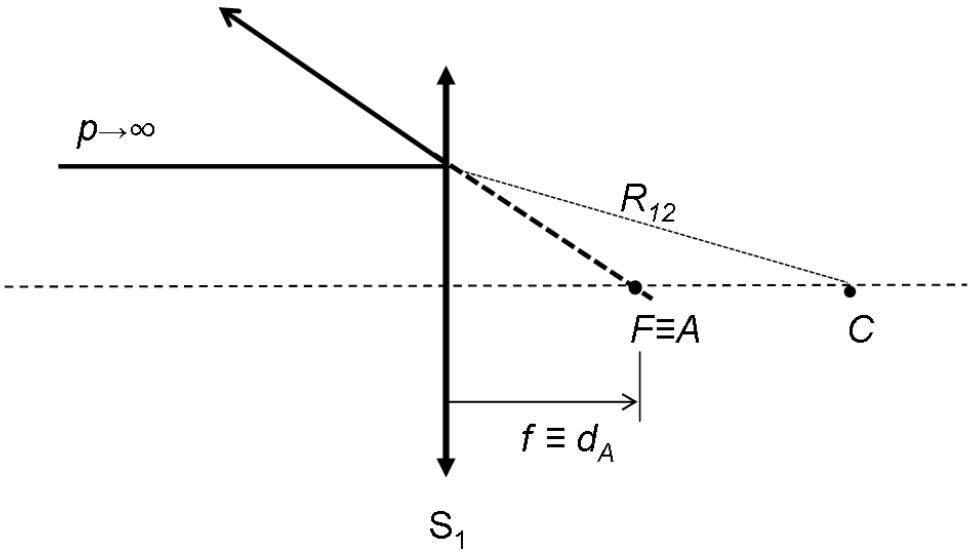

Figure 3.7: Reflected ray from S_1.

focus F acts as a virtual source, A. The distance of A from the vertex of S_1 is d_A and coincides with f. The formula 1.4 and 1.5 give us:

$$d_A = \frac{R_{12}}{2} \simeq 129\, mm \tag{3.6}$$

As concern the second reflection, we decompose the biconvex lens to three surfaces, as showed in Figure 3.8. While a part of the laser rays hitting the

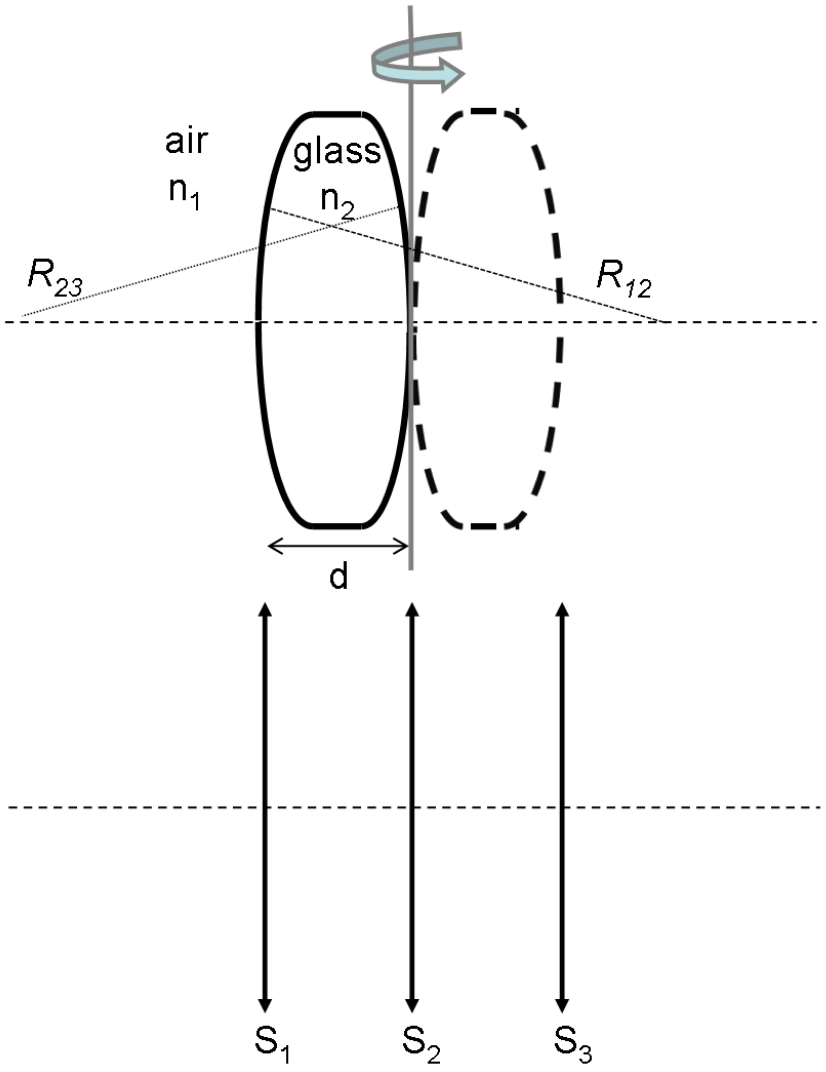

Figure 3.8: A thin lens has been broken into three surfaces.

first surface reflects, another refracts. We recall subsection 1.3.2. Refraction acts to focus all parallel rays to a point referred to as the principal focal point, F_2. The distance from the vertex of S_1 to F_2 is the focal length. By looking at the Figure 3.9 it is easy to understand that the focal length coincides with the image distance q_1. By using Snell's law we can find the refracted angle:

$$n_1 sin\alpha = n_2 sin\beta$$

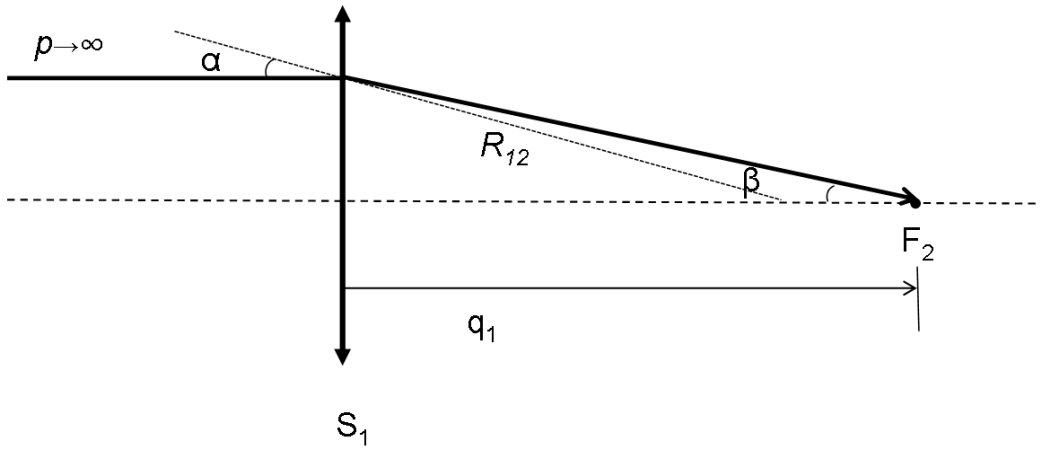

Figure 3.9: Refracted ray from S_1.

Since we uses Gaussian (or paraxial) approximation, we can expand the sin funcion up to the first order: $sin\alpha \sim \alpha$. So the refracted angle is $\beta = \alpha\frac{n_1}{n_2}$. By looking to the trigoniometry of the Figure 3.9, it is easy to obtain the focal lenght of the S_1:

$$R_{12}\tan\alpha = q_1\tan(\alpha - \beta)$$

. From

$$q_1 = \frac{R_{12}\alpha}{\alpha - \beta}$$

we get:

$$q_1 = \frac{R_{12}n_2}{n_2 - n_1} \simeq 774\,mm \tag{3.7}$$

Notice that we have found the formula 1.7.

Now we point out the second surface, S_2. The laser beam, after being refracted from S_1, reflects off S_2. Look at Figure 3.10. Since the refracted

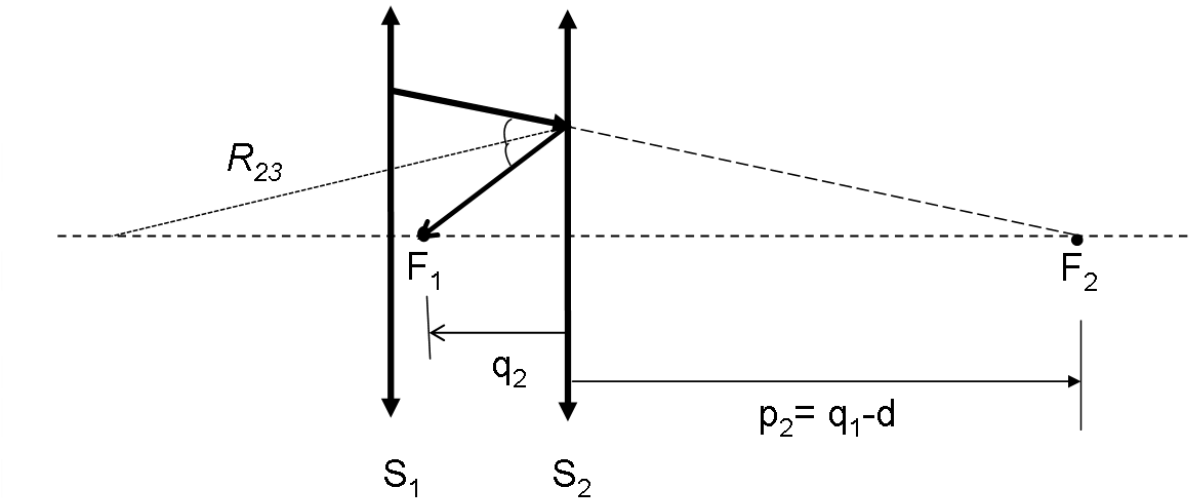

Figure 3.10: Reflected ray from S_2.

beam is not perfectly parallel to the optical axis, it does not convert to a common point, F, as expected from our considerations in subsection 1.3.1, but in F_1. In such a situation we remember the equation of conijugated point 1.4:

$$\frac{2}{R_{23}} = \frac{1}{p_2} + \frac{1}{q_2} \tag{3.8}$$

where $p_2 = -\mid q_1 - d \mid = -772\ mm$, because conventionally p_2 is on the right side of S_2. Approximately, by remembering that $R_{23} = -271\ mm$, we get $q_2 \simeq -115\ mm$.

Indeed, if we consider our model where S_2 is rotated 180 degree with respect to its vertical axis, the direction of the reflected ray will have to be modified as illustrated in Figure 3.11 and q_2 will become positive $q_2 \simeq +115$ mm. (conventionally the image distance is positive on the right side of S_2)

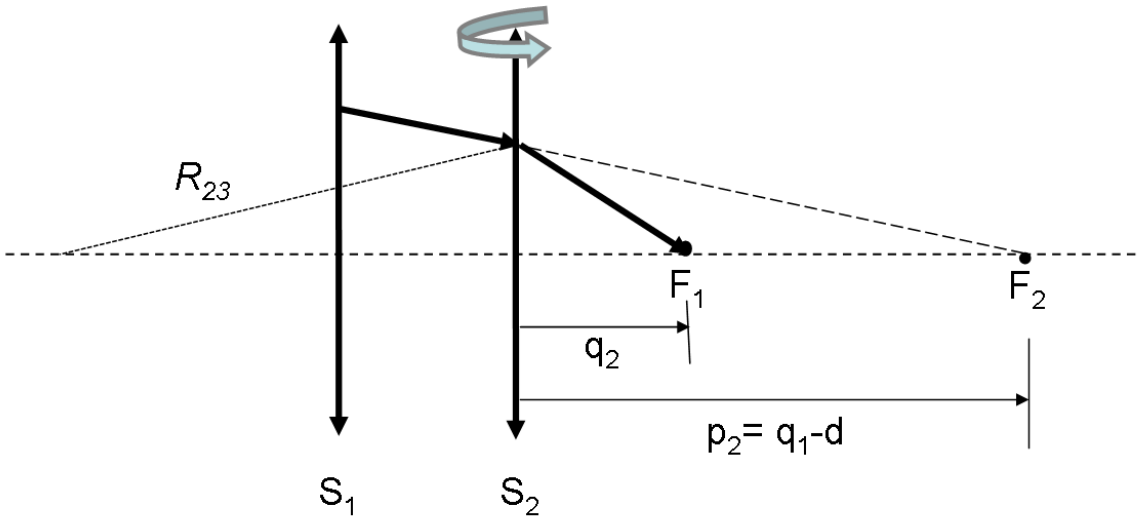

Figure 3.11: Reflected ray from S_2 in our model.

The laser rays reflecting off S_2 encounter S_3: the direction of these reflected rays change by refracting. So they focuses to B as in Figure 3.12. By referring to the formula 1.6:

$$\frac{n_2}{q_3} + \frac{n_1}{p_3} = \frac{(n_2 - n_1)}{R_{12}} \tag{3.9}$$

where $p_3 = - \mid q_2 - d \mid \simeq -113$ is negative because it is on the right side of S_3. So we get the image distance $q_3 \simeq 138\ mm$.

In this way the second reflection forms, by giving rise to a real image, B

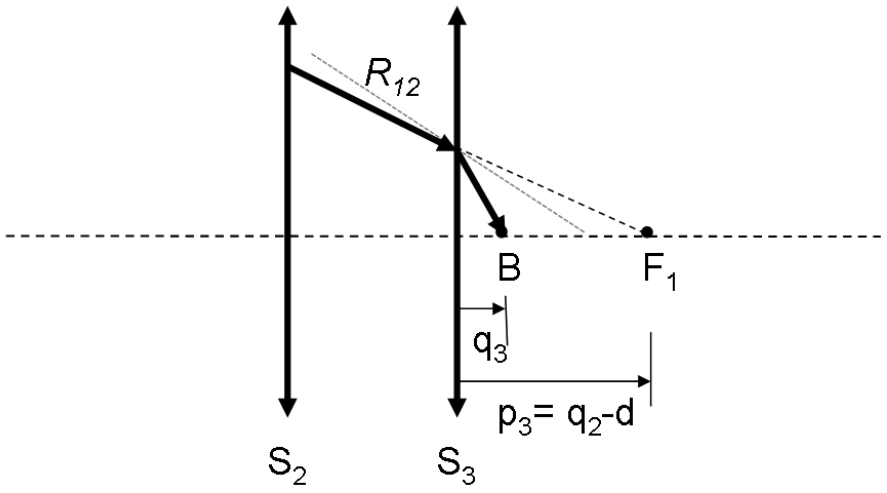

Figure 3.12: Refracted ray from S_3.

whose distance with respect to S_1 is d_B:

$$d_B = 2d + q_3 = 142\,mm \tag{3.10}$$

An overview of the second reflection is illustrated in Figure 3.13.

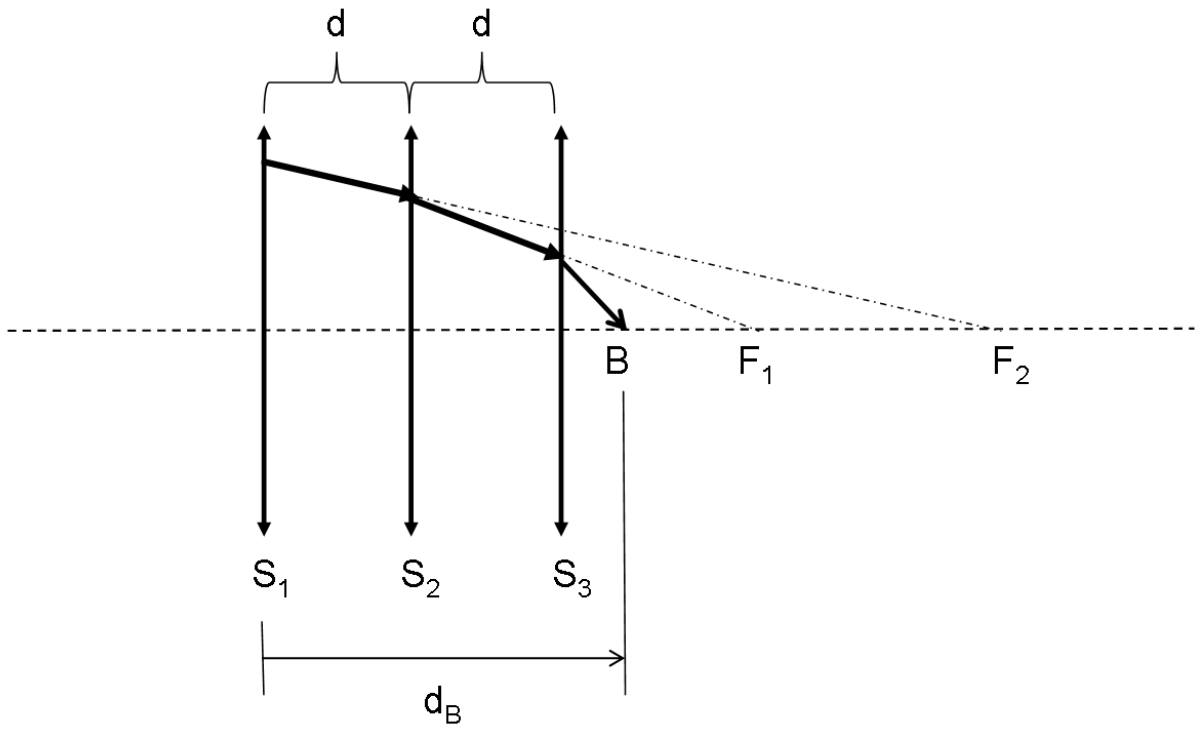

Figure 3.13: The distance of the real image B given by the biconvex lens.

In conclusion the interference of the two reflected rays, of A and B gives rise to Newton's rings and the optical system is consider to be aligned when the series of concentric circles are centered at the spot. Figure 3.14 illustrates the final aligned optical system.

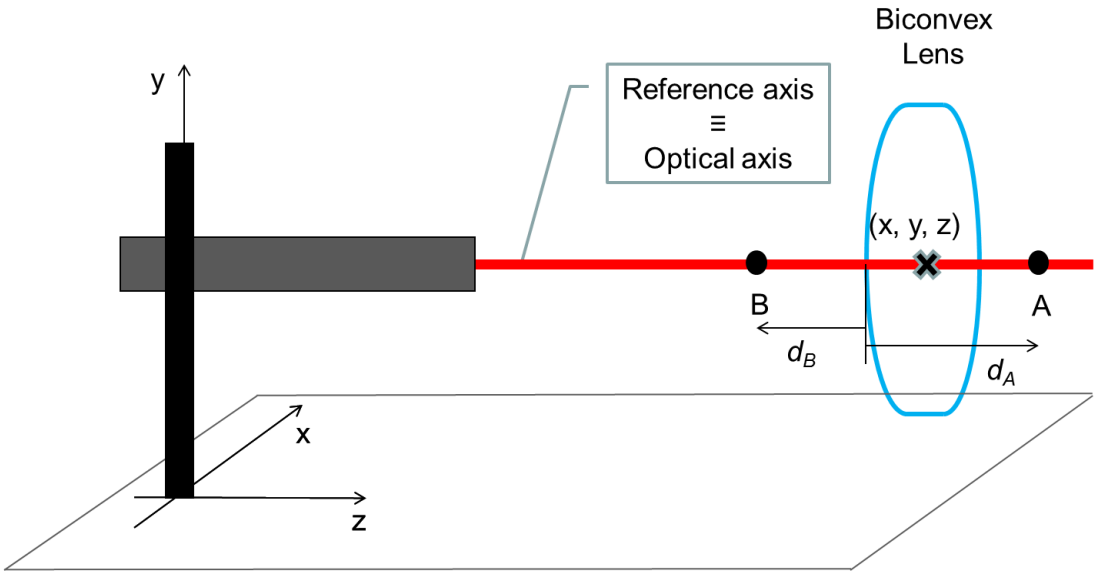

Figure 3.14: The position of centration of a biconvex lens.

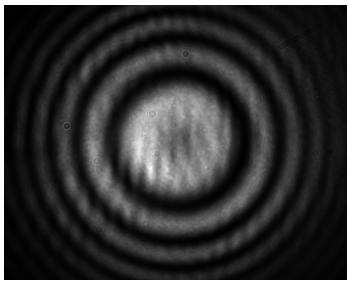

Figure 3.15: Newton's ring

Indeed it is impossible to achieve a perfect alignment: a tolerance range for the lens should be always taken into account.

Chapter 4

A simple verification of decentering

By referring to the previous demonstration of the formation of the Newton's rings in subsection 3.2.1, if we decenter the lens, specifically if we move the lens, from its position of centering, of the quantity Δy, the point A and B will move to the same quantity: $\Delta y_{A'} = \Delta y_{B'} = \Delta y$. Figure 4.1 shows that. Since

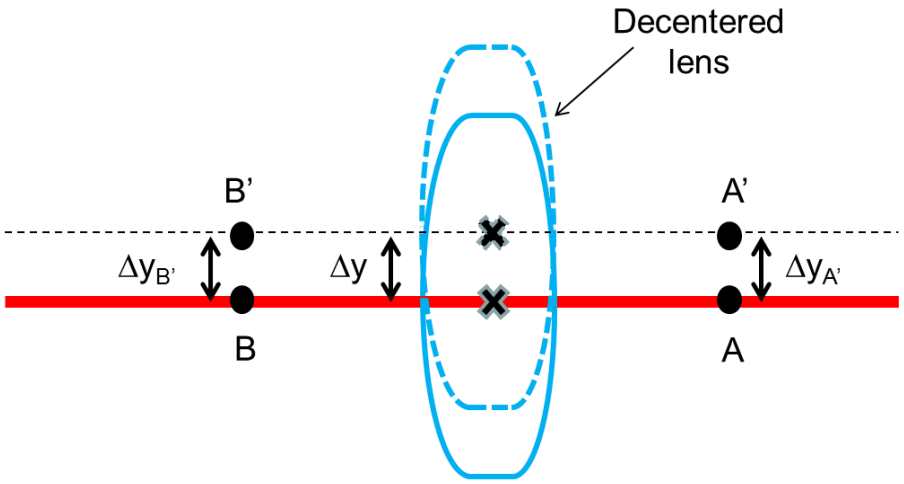

Figure 4.1: The displacement of the virtual source A and the real image B

the axis of Newton's rings is given by the projection of the line joining A and B, even the Newton's ring will move rigidly of Δy. We call the displacement of Newton's rings from the prolungation of the intersection of A and B: ΔN_y.

We would like to see the displacement of Newton's rings caused by the

decenter of a biconvex lens. From previous discussion it is easy to understand that, if we want to look at Newton's ring (as interference of two reflections) with a CCD, it is necessary a Beam Splitter to deviate the reflected rays coming from the lens.

4.1 Optical Setup

The steps we followed are:

- mounting of the laser
- materialization of the optical axis with the laser beam
- mounting and alignment of a beam splitter
- mounting of a biconvex lens
- mounting of a CCD.

4.1.1 Mounting of laser

As first step, we mounted the He-Ne laser on its support containing x, y displacements (green) and tip-tilt (yellow). The laser beam should be parallel

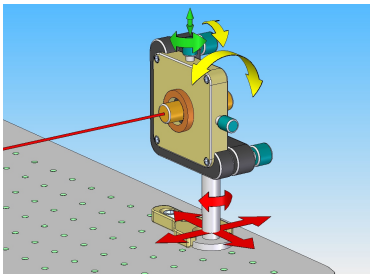

Figure 4.2: Laser support and its adjustments.

to the optical table and its height must be the one defined by centre of the other components. We chose 25.3 ± 0.1 cm (ruler's sensitivity, 1 mm). We fixed a ruler to the optical table parallel to one side and a graph paper on a support perpendicular to the optical table. This "graph paper support" could slide along the ruler fixed to the table. We placed it once far away from the laser and perpendicular to the laser beam and once more near the laser; we signed a cross + on the graph paper in correspondence to the height of the axis marked by the laser beam (in our case at height of 25.3±0.1 cm). We

adjusted the position in x, y and tilt of the laser until the laser beam hits the cross + in the both cases (both far away and near). Once the axis was set, we clamped the laser mount to the table. In this way the laser beam plays the role of reference axis for the other optics.

4.1.2 Mounting of Beam Splitter

We clamped the mechanical support of the Beam Splitter, BS, along the optical axis: it contains x, y displacements, a rotational movement along its axis and two other adjusters for tip-tilt. We mounted the BS on it such that the laser beam hits perpendicularly the centre of the BS's face. Figure 4.3. By using the back reflected, the transmitted rays and the adjustments we

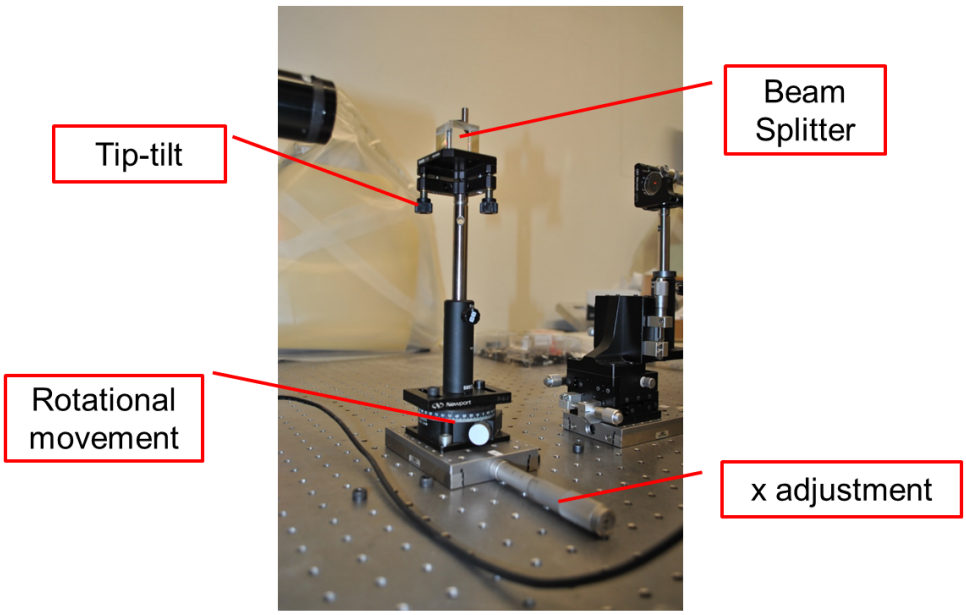

Figure 4.3: Beam Splitter and the adjustments.

aligned the BS: the reflected beam has to hit the centre of the laser and the transmitted beam has to coincide with the "cross" + of the "graph paper support". Figure 4.4.

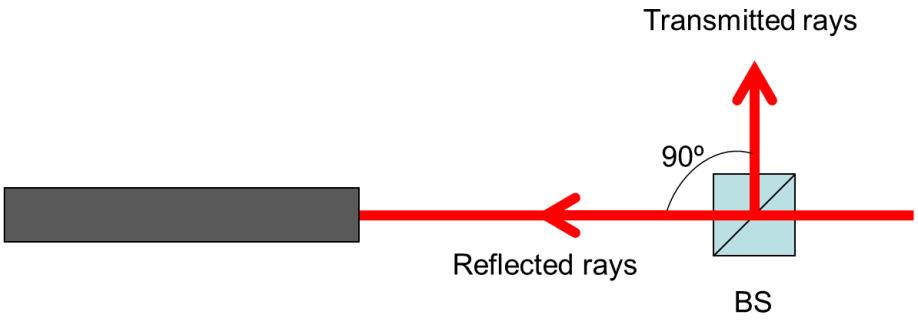

Figure 4.4: The alignment of BS.

4.1.3 Mounting of biconvex lens

We fixed the support of the lens on the optical table, along the optical axis, at $246 \pm 1\ mm$ of distance from the BS. We call l_1 this distance. The support contains two micrometres for x, y displacement and tip-tilt. We mounted the biconvex lens $01LDX341$ on it perpendicularly to the laser beam. Figure 4.6 shows the adjustments.

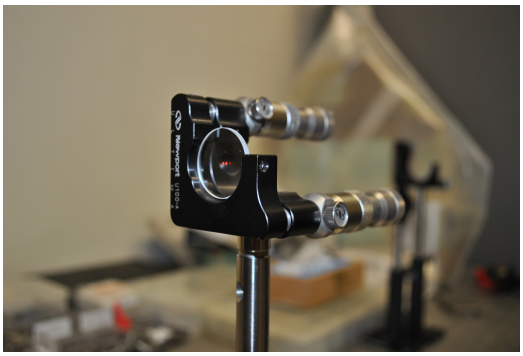

Figure 4.5: Biconvex lens

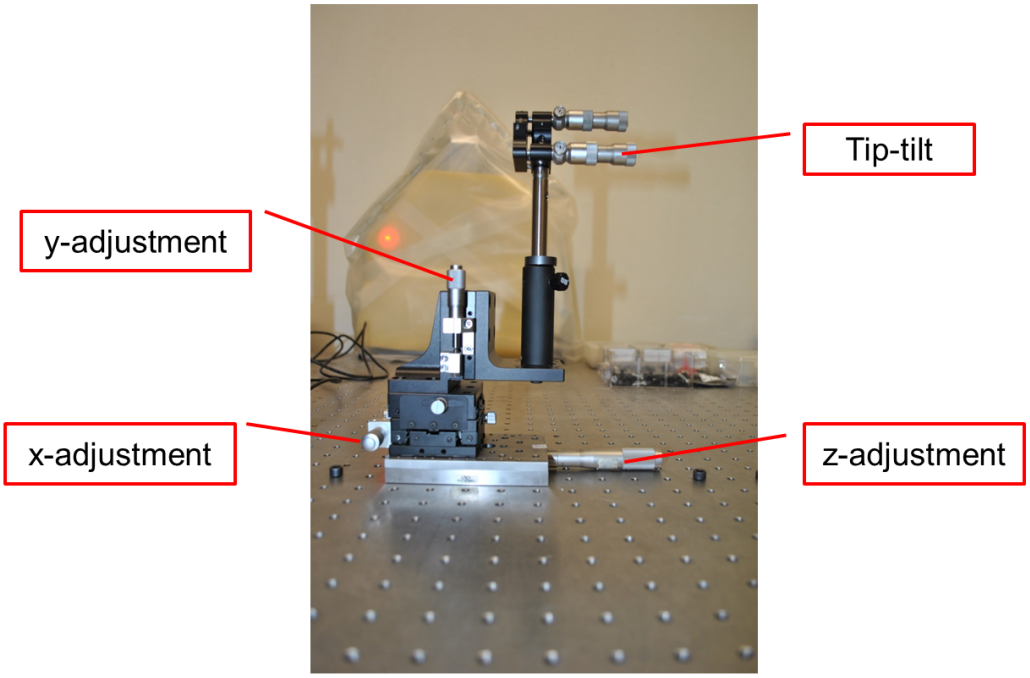

Figure 4.6: The adjustments of the biconvex lens' support.

The Table lists the main features of the lens $01LDX341$:

General Specification for 01LDX341	
Material	N-BK7
Focal length	200.0 mm
Radii of Curvature	$R_{12} = 258\ mm$, $R_{23} = -271\ mm$
Diameter	25.0 mm
Thickness	$d = 2.2\ mm$
Antireflection coating	$R_{avg} < 0.5\%$
Surface irregularity	$\lambda/2$
Surface quality	60.40

4.1.4 Mounting of CCD

The last step is to clamp the mechanical support of the CCD on the optical table in the position shown in Figure 4.7. We mounted the CCD on

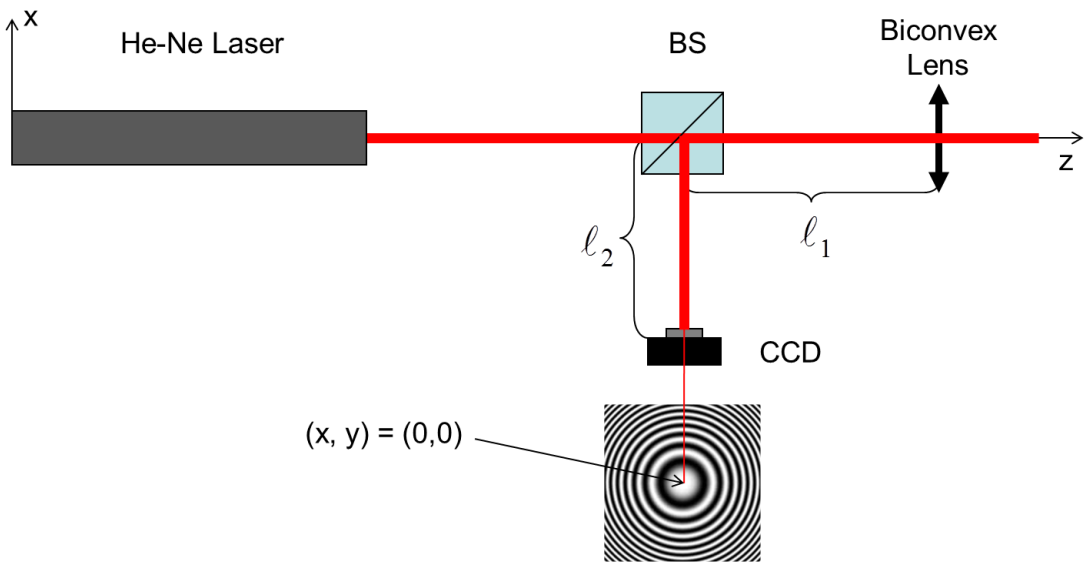

Figure 4.7: A scheme of the final optical setup

it, turned on the CCD and connected it to the pc. Obviously, the reflected rays has to hit the centre of the CCD such that we are able to see perfect or deformed Newtons rings when the lens is aligned or not respectively. The optical setup in laboratory is shown in Figure 4.8 with $l_1 = 246\,mm \pm 1$, $l_2 = 256\,mm \pm 1$ and a single pixel sixe is $p_x = 5.2 \times 5.2\,\mu m$.

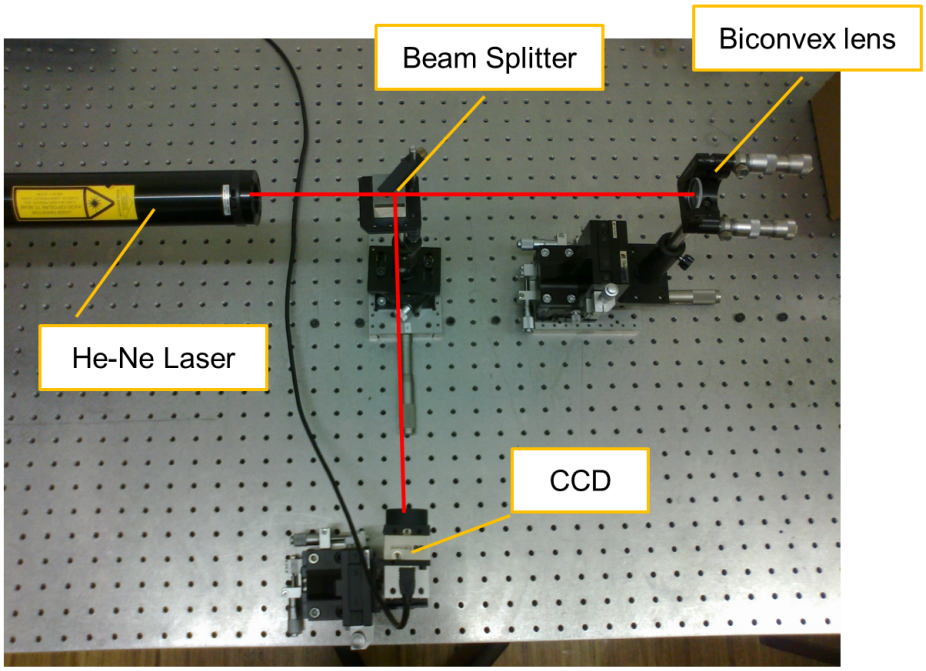

Figure 4.8: Final optical setup

4.2 Results in laboratory

In order to verify the theory above explained, we report some images captured with CCD and some measurements obtained in laboratory.

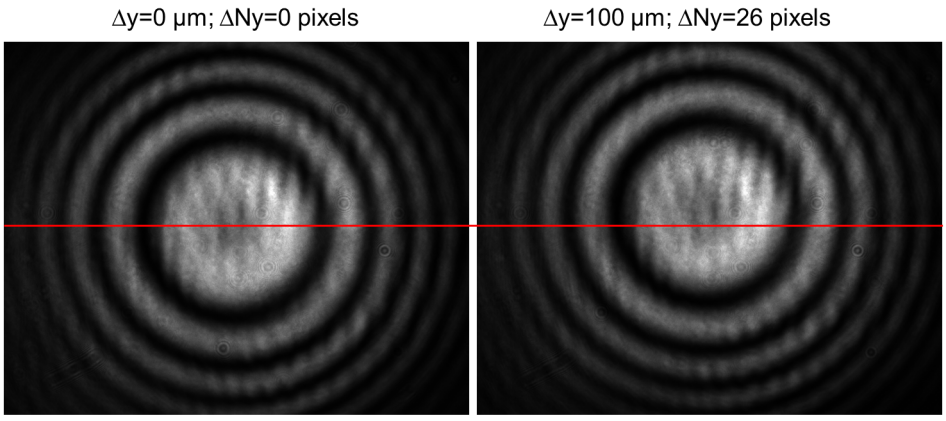

Figure 4.9: The displacement of Newton's ring caused by $\Delta y = 100\mu m$.

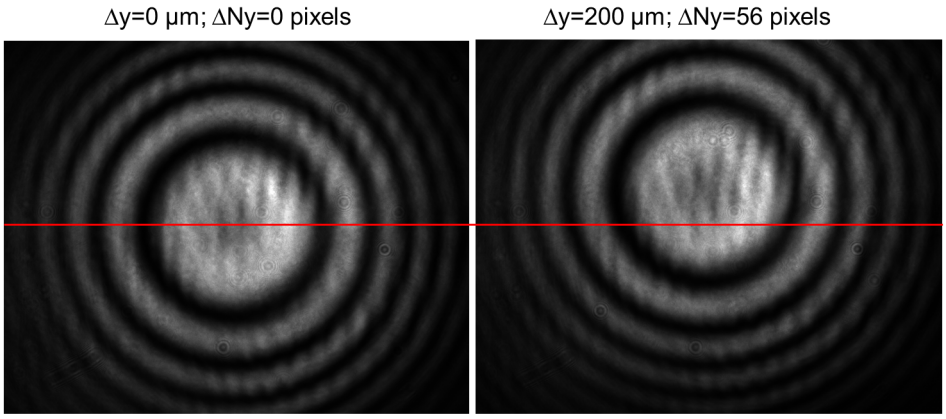

Figure 4.10: The displacement of Newton's ring caused by $\Delta y = 200\mu m$.

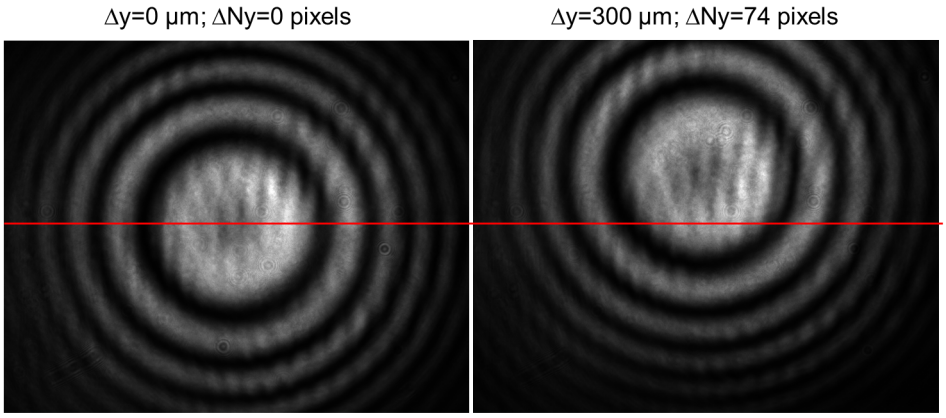

Figure 4.11: The displacement of Newton's ring caused by $\Delta y = 300\mu m$.

After mounting our optical setup as described previously, we calibrated the adjustment of the lens: we found that one mark of the micrometre corresponds to 10 $\mu m \pm 0.1$. Then, we looked at the image captured in the pc. We marked, with the mouse, a bullet • in the centre of the Newton's ring, in y_0. We decentered the lens by rotating the thimble of the micrometre of $100, 200, 300, 400, 500\mu m \pm 0.1$ always in the same direction. These decentering of the lens, Δy, causes a displacement of the Newton's ring with respect to its centre, ΔN_y: we measured these distances with the mouse by counting the pixels as ilustrated in the Figure 4.12. In the table 4.2 are listed, for each

decentering of the lens, these displacements of Newton's ring in pixels; we took 5 measures and we repeated the procedure three times.

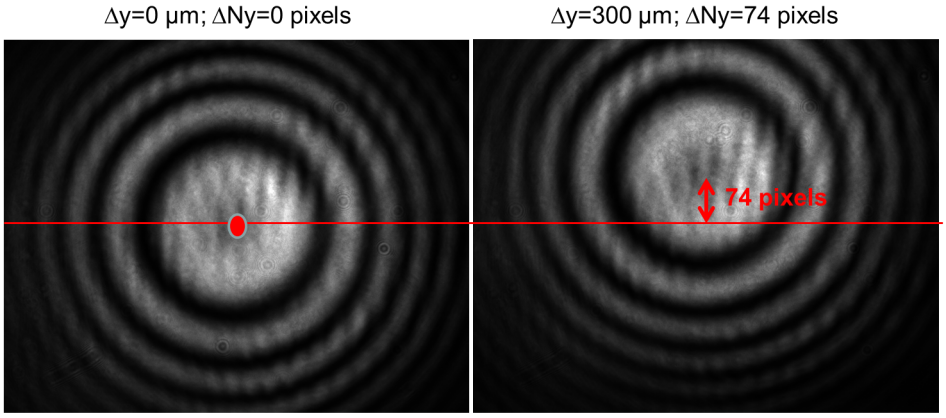

Figure 4.12: The measurement procedure of the displacement of Newton's ring, ΔN_y.

Δy (μm)	ΔN_y $(pixels)$	ΔN_y $(pixels)$	ΔN_y $(pixels)$
100 ± 0.1	26	28	30
200 ± 0.1	56	57	57
300 ± 0.1	74	73	75
400 ± 0.1	98	96	99
500 ± 0.1	122	120	124

The arithmetic mean, $<\Delta N_y>$ is reported in Table 4.2 with its standard deviation.

Δy (μm)	$<\Delta N_{y_i}>$
100 ± 0.1	28 ± 2
200 ± 0.1	56.7 ± 0.6
300 ± 0.1	74 ± 1
400 ± 0.1	97.7 ± 1.5
500 ± 0.1	122 ± 2

So, we can conclude that if we decenter the lens of a $\Delta y = 100\,\mu m$, we will see a displacement of the centre of the Newton's ring of about $< \Delta N_y >= 24.4\,pixels \pm 4.5$. Since one pixel is $5.2 \mu m$, then $< \Delta N_y >= 126.9\,\mu m \pm 23.4$.

Chapter 5

Discussion

An ideal optical system is called "nominal system": we would like to get it or, at least, to obtain the most similar one. In effect no optical system is perfectly aligned: errors of decentering and tilt have to take always into account.
Newton's rings are known since 1717, but only recently they are used to align the optical components.
We described how rays propagate in the lens used in laboratory by forming two virtual sources that interfere and form Newton's rings. This description allowed us to understand the relation between a vertical displacement of Newton's rings and the decentering of our lens.
We should have expected that ΔN_y would correspond to $\Delta N_y = 100\,\mu m$; in laboratory we have found $< \Delta N_y >= 126.9\,\mu m \pm 23.4$. The variance between the theoretical and experimental value is about $26.9\,\mu m$. It is a consistent error, which demostrates the validity of the linear relation between the decentering of the lens and the displacement of Newton's rings.
In this way, this thesis gives a theoretical approach to the fact that Newton's rings can be used for aligning all optical system.

5.1 Centering sensitivity

After having verified how the displacement of Newton's ring works with respect to the decentering of our lens, the latest goal of this thesis is to assess the alignment precision that must be fulfilled.
Since we have estimated (by eyes) a displacement of $< \Delta N_y >= 126.9\,\mu m \pm 23.4$ we can assert if our lens is centered with a certain precision.
So the last step is to identify how much the precision is; in other word we would like to assess the error of centration with the method of least square.

This method is a procedure to determine what the "best fit" line is to the data. The graphic 5.1 illustrates the data given in Table 4.2 and the "best fit" given by the linear equation (or linear regression) $\Delta N_{y_i} = mx + b$.

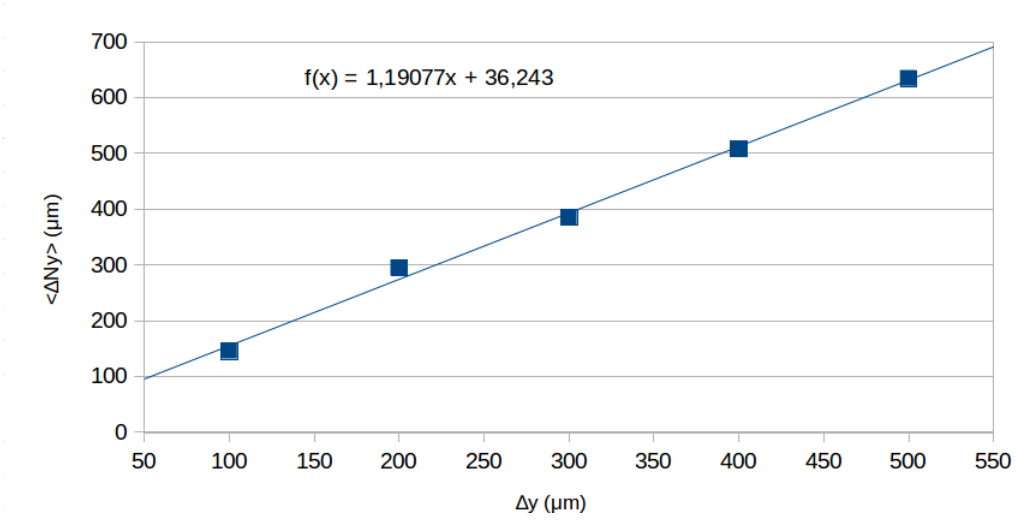

Figure 5.1: The displacement of Newton's ring with respect to the decentering of the lens.

The variance, $\sigma_{\Delta N_y}$, will measure how good of a fit we have that is the mean distance of the data from the linear regression. The variance for this data set is:

$$\sigma_{\Delta N_y} = \sqrt{\frac{1}{n-2}\sum_{i=1}^{n}(\Delta N_{y_i} - mx - b)^2} \tag{5.1}$$

In conclusion, we get:

$$\sigma_{\Delta N_y} = 2.8\,\mu m \tag{5.2}$$

Therefore the precision with whom the lens can be aligned is $2.8\,\mu m$.

5.1.1 Future perspective

This thesis has treated a theory about the decentering of a lens, which is truely confirmed by an experiment in the laboratory. Indeed, a system is referred to be aligned once both decentering and tip-tilt are adjusted. A suggestion for further thesis is to find out a relation between the tip-tilt of a lens and its corresponding displacement of Newton's rings and to demonstrate it with an optical setup similar to our.

Acknowledgements

I am thankful to Prof. Ragazzoni, who taught me many fascinating things about optics and passed his passion on to me. I am gratful to my parents Beatrice and Michele, my brother Alessandro and my cousin Sara for their wonderful support, whitout whom I will never succed in walking through this extraordinary path. A path rich of climb and descent, where my friends were (and are) always ready to help me, to encourage me during my frequent blackout. Of course, there was also thousand of funny and unforgettable moment with them! I would like to thank firstly Edo, who bore a schizophrenic girl from the first year of University to now (and I hope to still long time); Sofia for our undestructible and deep friendship despite the distances; Rosi and our fight to pass Analisys; my first roomate Michy who teach me to take decision and to be stronger; the Galileo group whit whom I grew like a baby with her mum; my erasmus friends in Heideberg and our little and special adventures; the "tangueri" and our common passion of dancing; and not for last, the "worst", who make me feel always at home when I am with them. The list would continue eternally!!!! So, I thank to each companion of travel who give me a piece of them.

List of Figures

Bibliography

[1] Frederick R. Chromey, "To Measure the Sky. An introduction to Observational Astronomy, (2011) Cambridge University Press

[2] Giorgia Gentile, "La camera Rossa per il Primo Fuoco del Large Binocular Telescope", (2005) Tesi di Laurea

[3] Mauro D'Onofrio, "Elementi di ottica per astronomi", (2012) Cleup

[4] "Large Binocular Telescope Observatory", http://www.lbto.org/index.htm

[5] E. Diolaiti, R. Ragazzoni, F. Pedichini, R. Spezialid et al, "Blue and red channels of LBC: a status report on the optics and the mechanics", (2003) SPIE Vol. 4841

[6] D. Magrin, R. Ragazzoni, C. Arcidiacono; S. Basso; M. Dima; J. Farinato et al, "PLATO: detailed design of the telescope optical units", (2010) SPIE Vol. 7731